

Influence of Finite Span and Sweep on Active Flow Control Efficacy

David Greenblatt*

Technion – Israel Institute of Technology, Technion City, 32000, Haifa, Israel

Anthony E. Washburn†

NASA Langley Research Center, Hampton VA 23681-2199

Active flow control efficacy was investigated by means of leading-edge and flap-shoulder zero mass-flux blowing slots on a semispan wing model that was tested in unswept (standard) and swept configurations. On the standard configuration, stall commenced inboard, but with sweep the wing stalled initially near the tip. On both configurations, leading-edge perturbations increased $C_{L,max}$ and post stall lift, both with and without deflected flaps. Without sweep, the effect of control was approximately uniform across the wing span but remained effective to high angles of attack near the tip; when sweep was introduced a significant effect was noted inboard, but this effect degraded along the span and produced virtually no meaningful lift enhancement near the tip, irrespective of the tip configuration. In the former case, control strengthened the wingtip vortex; in the latter case, a simple semi-empirical model, based on the trajectory or “streamline” of the evolving perturbation, served to explain the observations. In the absence of sweep, control on finite-span flaps did not differ significantly from their nominally two-dimensional counterpart. Control from the flap produced expected lift enhancement and $C_{L,max}$ improvements in the absence of sweep, but these improvements degraded with the introduction of sweep.

* Senior Lecturer. Faculty of Mechanical Engineering. Senior Member. davidg@technion.ac.il

† Branch Head, Flow Physics and Control Branch. Senior Member. Anthony.E.Washburn@nasa.gov

Nomenclature

AR	= wing aspect ratio
c	= model chord-length
C_d	= sectional form-drag coefficient
C_D	= model form-drag coefficient
C_l	= sectional lift coefficient
C_L	= model lift coefficient
C_m	= sectional moment coefficient
C_M	= model moment coefficient
C_R	= model rolling moment coefficient
C_Y	= model yawing moment coefficient
C_p	= time-mean pressure coefficient
C_μ	= slot momentum coefficient, $h/c(U_j/U_\infty)^2$
f	= separation control excitation frequency
F^+	= reduced excitation frequency, fX/U_∞
h	= slot width
L_f	= flap length, from slot to trailing-edge
p'	= rms pressure fluctuations in the wing plenum
q	= free-stream dynamic pressure
Re	= Reynolds number based on chord-length
s	= wing semispan length, $b/2$
U_j	= average peak jet slot blowing velocity
U_∞	= free-stream velocity
U_ϕ	= phase velocity of the fundamental pressure perturbation
U, V, W	= mean velocities in directions x, y, z
X	= distance from perturbation to wing trailing-edge
x, y, z	= coordinates measured from model leading-edge and root (left-hand system)
α	= angle of attack
α_s	= static stall angle
δ	= flap deflection angles, $(\delta_i, \delta_o, \delta_t)$
Λ	= sweep-back angle

Subscripts

i	= inboard
fs	= flap-shoulder
le	= leading-edge
n	= normal to the leading-edge
o	= outboard
sw	= conditions on the swept wing
t	= tip, tangential to the leading-edge
te	= trailing-edge

I. Introduction

The capability and limitations of zero mass-flux active flow control (AFC) are reasonably well understood in relatively simple two-dimensional flows and on airfoils [1]. Thus for high aspect ratio unswept wings, first order performance approximations can be made directly. However, for low aspect ratio wings – for example on combat, unmanned and micro vehicles, and control surfaces – significant three-dimensional effects preclude direct extensions of two-dimensional results. Currently very little is known about the efficacy of AFC in conjunction with three-dimensional effects, for example near wingtips and flap edges, where the flow becomes strongly three-dimensional due to an abrupt change in the spanwise geometry [2]. With the introduction of sweep, these tip and edge flows become further complicated, and are prone to premature separation [3,4].

The vortex systems existing on a wing at incipient stall play a defining role in the mechanism of lift enhancement via control. An unswept wing of constant chord (rectangular planform) is expected to stall inboard where the loading is the greatest and because of the near two-dimensionality of this flow, it is expected that stall will resemble that on its corresponding profile (airfoil), with all its attendant characteristics. Two of the most common stalling mechanisms are relatively gentle trailing-edge stall [5] and leading-edge bubble bursting mechanisms which often manifests as quasi-periodic shedding of dynamic stall vortices [6-8]. Common observations in the vicinity of stall are hysteresis, i.e. the flow state depends on whether α is increasing or decreasing, and bi-stable flow states. As the wingtip is approached, loading decreases as expected, but the vortex rollup on a rectangular planform wings with square tips exhibit characteristics far removed from basic assumptions of lifting line theory [9], even for high aspect ratio configurations [10]. At conditions approaching stall, a principal feature is the significant rollup of a main vortex and an aft secondary counter-rotating vortex on the upper surface adjacent to the wingtip [9-11]. Active separation control in the tip region of unswept constant chord configurations has never been performed, most probably because stall commences inboard, while the flow in the tip region remains seemingly attached and therefore considered secondary from a control perspective. A detailed study of post-stall behavior [12] indicated that lift in the tip region continues to increase in the presence of inboard stall, but this is accompanied

by large local pressure drag and nose-down pitching moments. Moreover, hysteresis associated with inboard stall is dramatically reduced in the tip region. This is most probably due to the relatively stable nature of the tip vortex system.

With the introduction of sweep, a number of new factors become relevant. In addition to the common inflectional and centrifugal instabilities, leading-edge control may be affected by crossflow and attachment line instability mechanisms [13]. At angles of attack approaching stall, separation is expected to occur near the wingtips for two reasons. Firstly, sweep increases outboard loading, thereby promoting separation near the tip [14] and secondly, the pressure gradient normal to the flow direction drives the boundary layer towards the tip, thereby producing a thicker boundary layer that is more prone to separation [3]. It appears that no systematic study has been undertaken of how these factors affect the efficacy of separation control. Nevertheless, the effect of infinite sweep on control at the flap shoulder was studied [15] and sweep transformations were defined based on the flow and dimensions normal to the leading-edge. Apart from the upper surface reattachment zone, this resulted in a reasonable congruence collapse of the swept and unswept data sets. Similar observations were made in the separated region produced by a hump on the wall of a wind tunnel [16]. Nevertheless, the efficacy of control in the presence of finite span flaps on swept wings has not been studied.

Significant attention has been given to control on thin delta wings, where flow separates at the leading-edges and rolls up into so-called leading-edge vortices, that generate lift at low speeds. Prior to stall, axial flow in the leading-edge vortices has a stabilizing influence [17-19]. However, when the swirling momentum exceeds the axial momentum by approximately 30% (swirl-number~1.3), the vortex “breaks down,” i.e. it becomes highly diffuse and unsteady, and the swirling and longitudinal (or axial) velocities reduce dramatically [20]. This well-known, but only partially understood, phenomenon has been the subject of numerous investigations [20] and the object of many control attempts [20-28]. The vast majority of studies indicated an optimum reduced frequency in the approximate range: $1 \leq F^+ \leq 2$, based on the velocity and largest dimension normal to the leading-edge [22-28]. In analogy with two-dimensional shear layers, it appears that periodic excitation introduces “instability driven large eddies which periodically transport high momentum fluid to the surface” [23] and increase the post-stall normal force on

the wing. Nevertheless, the relationship of this mechanism to vortex breakdown is unclear, with speculations ranging from delay of vortex breakdown [25], to vortex enhancement [27], to reconstitution of the vortex [22].

In the present investigation, an attempt was made to systematically study three-dimensional effects by designing and testing an active flow control semispan model in unswept (standard) and swept configurations. The model was equipped with a leading-edge slot and three identical simple flaps with individual control slots. The model could also incorporate arbitrary wingtip designs. The overall strategy was to introduce successively larger three-dimensional effects, starting with the relatively innocuous unswept configuration, followed by individual flap deflections, the introduction of sweep and finally the introduction of sweep combined with flap deflections. Control was introduced via zero mass-flux blowing slots at the leading-edge and flap-shoulder. Surface pressure ports, integrated to yield wing loads, were used to gauge the efficacy of control.

II. Experimental Setup & Testing

A. Semispan Model Description

Low speed AFC experiments were performed on a rectangular planform semispan NACA 0015 model ($AR=4$; semispan $s=609.6\text{mm}$, chord $c=304.8\text{mm}$). The model incorporated three identical simple flaps of span $s_f = \frac{1}{3}s$ hinged at $0.7c$ (*inboard*, *outboard* and *tip*; fig. 1a) and was equipped with leading-edge and flap-shoulder flow control slots, joined to interior plenums (fig. 1b). The leading-edge slot ($h=5.08\text{mm}$) was located at $x/c=0$ and was oriented so as to produce a wall-jet-type perturbation, nearly parallel to the surface. The flap slots (all $h=7.62\text{mm}$) were also configured to produce wall-jet-type perturbations, parallel the upper surface corresponding to the un-deflected flap direction. Flaps were deflected in unison and also deflected individually to assess the effects of three-dimensionality. The notation $\mathcal{E}(\delta_i, \delta_o, \delta_t)$ is used throughout to indicate the particular configuration under consideration. Forcing was supplied to the plenums via voice-coil based actuators [ATEAM (Aero and Thermally Engineered Actuator Modules) designed and manufactured by J. Kiedaisch, H. Nagib and their associates from IIT]. The resultant zero mass-flux control slot velocities were calibrated using a hot wire anemometer for the frequency range $40\text{Hz} \leq f \leq 400\text{Hz}$ along the span of the wing. Uncertainty in the perturbation amplitude was

estimated at $\Delta C_\mu/C_\mu \pm 10\%$, based on the hot wire calibration uncertainty and uncertainty associated with the precise location of the hot-wire within the jet “top-hat” region. The C_μ values cited in this paper are all based on the center-span calibration location, $y/s=0.5$. Appendix A provides additional details relating the slot calibration and its associated uncertainties.

The model was equipped with 165 static pressure ports arranged in a perpendicular spanwise and chordwise grid (fig. 1c), with additional rows of pressure ports on the flaps. A three-dimensional interpolation scheme was employed to improve local surface pressure estimates (see Appendix B) and the surface pressures were integrated to estimate aerodynamic loads. The model was also equipped with unsteady pressure transducers: nine were mounted on the wing upper surface and three are mounted within the wing plenums to monitor control frequencies and amplitudes. Steady and unsteady wing surface pressure data were acquired for angles of attack $\alpha \leq 33^\circ$ and flap deflection angles of $0^\circ \leq \delta \leq 40^\circ$. Wing static pressures were measured using a high-speed pressure scanner and unsteady pressures were measured by means of piezoresistive unsteady pressure transducers. The main source of error in the pressure measurements was due to precision, with $C_p \leq \pm 0.02$, based on 95% confidence intervals.

The wing was tested in both a “standard” (unswept) configuration (see figs. 1a-1c; photograph in fig. 1d) and a “swept” configuration (see figs. 2a-2c; photograph in fig. 2d), where control perturbations were supplied from both slots. Sweep was achieved by means of a triangular wedge, also with a NACA 0015 profile, which was also instrumented with pressure ports (figs. 2a-2c). Furthermore, various tip extensions were tested, namely: (a) “no tip extension” and (b) a square tip extension for the standard configuration (figs. 1a and 1b respectively); and (a) “no tip extension,” (b) square tip and (c) parallel tip extensions for the swept configuration (figs. 2a-2c respectively). The wingtip extensions were not instrumented with pressure ports. In the swept configuration, flap deflection resulted in a gap between the inboard edge of the inboard flap and the tunnel wall (see photograph in fig. 2d, where all flaps are deflected to 20°). A removable fairing was employed to seal the gap and its effect on control effectiveness was also considered.

Due to limitations associated with the α traversing system, data were acquired in the ranges $-4^\circ \leq \alpha \leq 17^\circ$ and $15^\circ \leq \alpha \leq 33^\circ$. In the lower range, data at even angles are for α increasing and odd

angles are for α decreasing, and vice versa in the higher range. This convention was applied consistently throughout this paper. The overlap of 2° between the two ranges, namely $15^\circ \leq \alpha \leq 17^\circ$, facilitated a check on the repeatability and consistency of all data. Unless otherwise specified, the tunnel was always brought to the test conditions with the wing located at the minimum α . Furthermore it is noted that, due to physical limitations of the setup, the angle $\alpha=33^\circ$ was not exceeded.

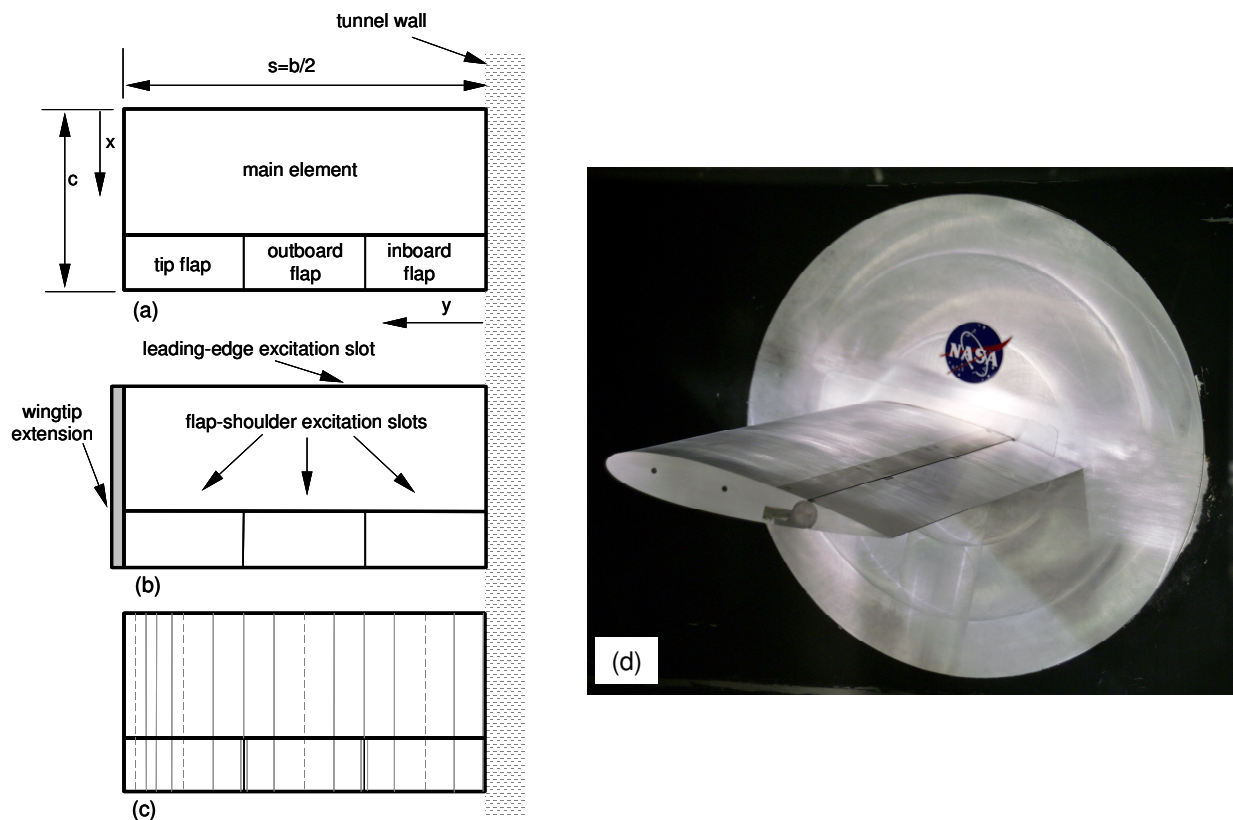


Fig. 1. Schematics of the unswept (standard) semispan configuration, showing (a) wing components and left-hand coordinate system with no tip extension; (b) locations of the control slots and the wingtip extension; (c) locations of the pressure ports on the main-element and flap. Fig. 1d. Photograph of the unswept semispan wing in the Basic Aerodynamics Research Tunnel (without the wingtip extension).

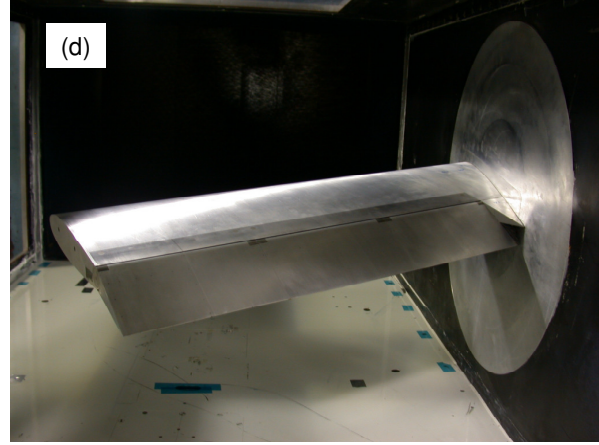
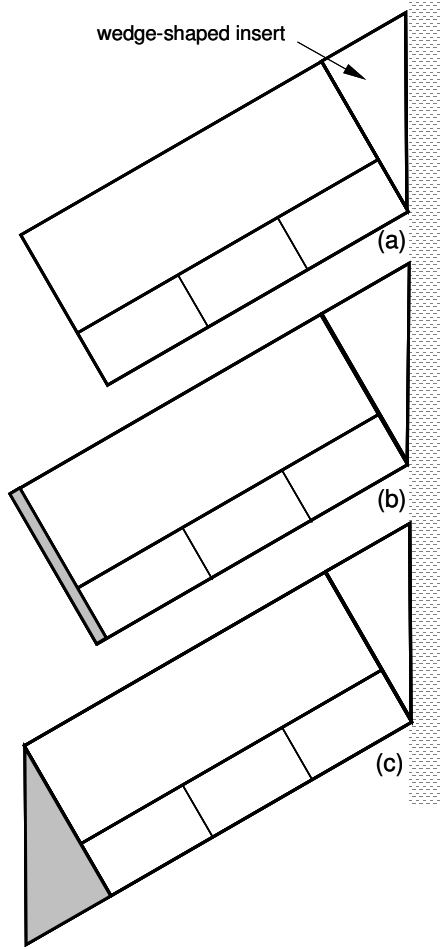


Fig. 2. Schematics of the swept semispan configuration, showing (a) no wingtip extension; (b) the square wingtip extension; and (c) the parallel wingtip extension. Fig. 2d. Photograph of the swept semispan wing in the Basic Aerodynamics Research Tunnel (without wingtip extensions).

B. Data Reduction

With the introduction of sweep, pressure data was analyzed with respect to the velocity component normal to the wing leading-edge (cf. [2]). This facilitated a direct comparison of corresponding surface pressures for the standard and swept configurations. Since the wing is cantilevered, the infinite sweep relations are modified to account for the variable angle of attack, thus:

$$\Lambda' = \arctan(\tan \Lambda \cos \alpha) \quad (1)$$

and hence the velocity component normal to the leading is

$$U_{\infty,n} = U_{\infty} \cos \Lambda'. \quad (2)$$

Substituting this relation into the definition for two-dimensional pressure coefficient, gives

$$C_{p,n} = C_{p,sw} / \cos^2 A' \quad (3)$$

The AFC parameters were also modified to account for the cantilevered and swept wing, thus:

$$C_{\mu,n} = C_{\mu,sw} / \cos^2 A' \quad (4)$$

$$F_n^+ = F_{sw}^+ / \cos A' \quad (5)$$

For convenience and brevity the subscript n in equations (2)-(5) is dropped from the remaining parameters in the following discussions, but is always implied for the swept configuration. The definition of A' in eqn. (1) above, requires a small variation in f and U_p at every α in order to maintain constant $C_{\mu,n}$ and F_n^+ , but this did not prove to be practical. Therefore, these parameters are always cited for $\alpha=0^\circ$ and it is understood that they are over-predicted by maximum values of 8% and 4% respectively at $\alpha=33^\circ$.

C. Three-Dimensional Configurations & Strategy

In an attempt to introduce three-dimensional effects gradually, a graded approach was adopted, and the study was divided into four categories. A: standard and swept configurations with leading-edge control, with and without flap deflections; B: combined control from the leading-edge and flap-shoulder (discussed in ref. [7]); C: the deflection of individual flaps with control at the shoulder; and D: sweep combined with flap-shoulder control. More details regarding the configurations and section references can be found in table 1.

Table 1. Details of the different configurations tested in the present study.

Cat.	$(\delta_i, \delta_o, \delta)$	control location	wing configuration	tip configuration	section/ref.
A	$(0^\circ, 0^\circ, 0^\circ)$	leading-edge	standard/swept	no extension/ with extension/ parallel tip	III.A.1 – III. A.4
A	$(20^\circ, 20^\circ, 20^\circ)$	leading-edge	standard/swept	no extension/ with extension/ parallel tip	III. A.5
A	$(40^\circ, 40^\circ, 40^\circ)$	leading-edge	standard/swept	no extension/ with extension/ parallel tip	III. A.5
B	$(20^\circ, 20^\circ, 0^\circ)$	combined	Standard	no extension/ with extension	see ref. [7]
B	$(20^\circ, 20^\circ, 20^\circ)$	combined	Standard	no extension/ with extension	see ref. [7]
B	$(40^\circ, 40^\circ, 40^\circ)$	combined	Standard	no extension/ with extension	see ref. [7]
C	$(20^\circ, 20^\circ, 0^\circ)$	flap-shoulder	standard/swept	no extension	III.B.1
C	$(20^\circ, 0^\circ, 0^\circ)$	flap-shoulder	standard/swept	no extension	III.B.1
C	$(0^\circ, 20^\circ, 0^\circ)$	flap-shoulder	standard/swept	no extension	III.B.1
D	$(20^\circ, 20^\circ, 20^\circ)$	flap-shoulder	swept	no extension/ with extension/ parallel tip	III.B.2
D	$(40^\circ, 40^\circ, 40^\circ)$	flap-shoulder	swept	no extension/ with extension/ parallel tip	III.B.2

III. Discussion of Results

A. Stall Mechanism and Leading-edge Control

Preliminary data was acquired at $Re=500,000$ and $Re=1,000,000$ for the standard (unswept) configuration without flap deflections or wingtips, and these data sets were compared with other investigations conducted at $1,800,000 \leq Re \leq 2,000,000$ and $AR=6.6$ [10,11]. Despite the larger Reynolds numbers and aspect ratios, the pressure distributions were similar inboard and outboard near the wingtip (see a comparison at $\alpha=12^\circ$ in appendix B, fig. B3). The similarity of the inboard pressure distributions indicated indirectly that boundary layer transitions were similar in the different investigations. It was speculated that the discontinuity created by the open leading-edge slot downstream of the stagnation point, effectively tripped the boundary layer, but this was not verified by direct boundary layer measurements. The similarity of the pressure distributions at the tip, showing three distinct, pressure peaks is remarkable, considering the different conditions of each experiment (see fig. B3a); the reason for these peaks is discussed in section III.A.3 below. It was further shown in [10] that, providing the wingtip is square, the flow in the tip region is effectively Reynolds number independent. It appears that the sharp lower edge of the square wingtip fixes the separation point independent of Re . For round wingtips, this is certainly not the case as shown in [10].

Baseline and controlled wing lift coefficient data are shown for both standard and swept configurations (fig. 3), with no wingtip extension installed (cf. schematics in figs. 1a and 2a). For both configurations, aerodynamic coefficients were based on the rectangular part of the planform only, i.e. pressure measurements on the wedge-shaped insert were not included in the sweep lift and drag calculations. In both instances, leading-edge control was applied at $F^+ = 0.65$ and $C_{\mu}=0.3\%$, although the physical frequencies and jet amplitudes were different to account for sweep (see eqns. 4 and 5). The choice of this reduced frequency was based on a number of considerations. Firstly, previous investigations on a NACA0015 airfoil with a similar leading-edge slot [12,10] established an optimum $F^+ \sim 0.6$ that was Reynolds number independent. Secondly, a similar observation was made on the present model and is shown in ref. [2]. Thirdly, the physical frequency used here, namely 52.5Hz, showed the smallest spanwise distortion of all frequencies considered, with a 10% variation across the span.

The standard baseline configuration appears to stall at $\alpha \approx 18^\circ$ and exhibits significant post-stall hysteresis (a bi-stable flow), that is generated inboard (as discussed below). The application of leading-edge control effectively eliminates hysteresis, which is routinely observed on two-dimensional (airfoil) configurations, and $C_{L,max}$ is attained at $\alpha \approx 25^\circ$. The swept baseline configuration stalls very gently at $\alpha > 20^\circ$ and, in contrast, shows very little hysteresis. It can be assumed that the axial flow component stabilizes the separated vortical flow near the leading edge, much like axial flow stabilizes leading-edge and “trapped” vortices [17]. With the application of control, the wing continuously generates lift with α , albeit at low $dC_L/d\alpha$, and appears to be still increasing at $\alpha = 33^\circ$ (maximum attainable with the present setup). For both configurations, control increases $C_{L,max}$ by approximately 0.23. Due to the partially stalled nature of the flow, however, these post stall increases are accompanied by large drag increases. It was noted that control applied at pre-stall angles of attack had virtually no effect on the surface pressures, and this observations is fully consistent with airfoil data [1]. Henceforth, control was not applied under conditions where separation was not present.

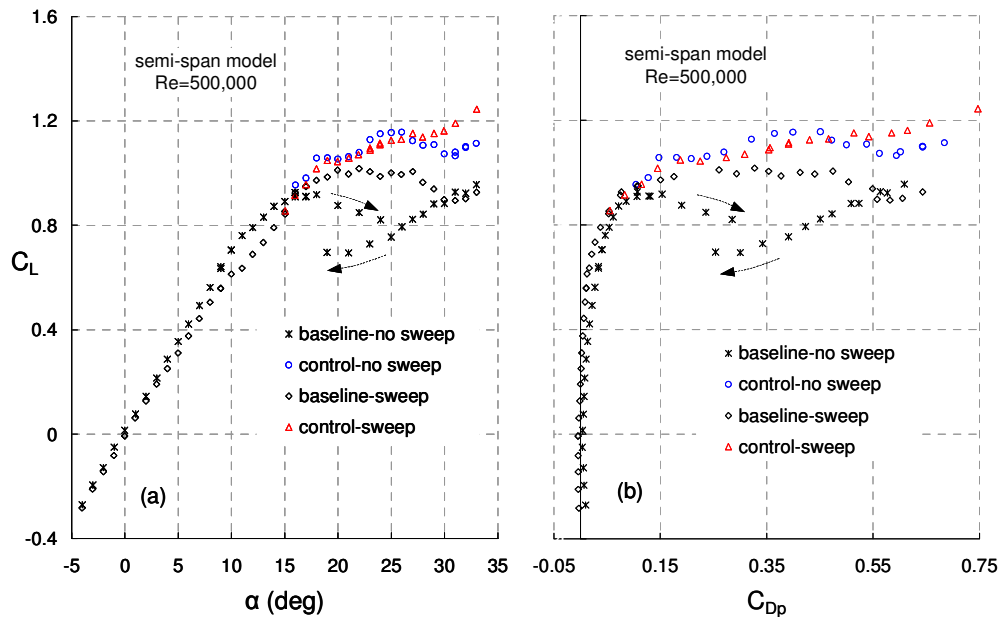


Fig. 3. Wing lift and form-drag coefficients based on integrated pressures on the rectangular section of the model (see fig. 1c). (No wingtip extensions.) Control at $F^+ = 0.65$ and $C_\mu = 0.3\%$.

1. Comparison of Baseline Stall Mechanisms

A preliminary assessment of the spanwise stall mechanisms for both configurations can be made by considering figs. 4a and 4b respectively. For the standard configuration, incipient stall is evident inboard, close to the tunnel wall, at $\alpha = 14^\circ$. However, the loss of lift inboard, evident for $\alpha > 14^\circ$, is accompanied by an increase in lift outboard, and this continues with increasing angle of attack (fig. 4a). The distortion of the load distribution near the tip of the wing ($y/s > 0.97$) is due to the formation of vortex at the wingtip and these measurements are fully consistent with data of other investigations (e.g. [10,11]) at higher Reynolds numbers. Inboard stall, accompanied by continued outboard lift increases, results in an overall lift increase and the perceived wing stall is at $\alpha \approx 18^\circ$ (fig. 3a). This stall scenario is fully consistent with a previous investigation of static and dynamic stall at $Re > 2,000,000$ and $AR = 10$ [12]. With sweep, significantly more lift is generated inboard, but this is offset by the poor outboard lift generation (fig. 4b). Between $\alpha = 17^\circ$ and 19° , changes to lift are negligible near the tip and stall is observed at $\alpha \approx 21^\circ$. Thus, when compared to the unswept case, the stall mechanism is reversed with lift continuously increasing inboard. The stall mechanisms (inboard for the standard configuration and outboard for sweep), when integrated over the span, manifests as the relatively gently wing stall observed in figs. 3a and 3b.

More evidence of the stall mechanism is provided by the surface pressure coefficient data shown for $\alpha = 14^\circ$ at selected spanwise locations ($y/s = 0.17, 0.5, 0.83, 0.99$) in figs. 5a to 5d respectively. No interpolation was necessary at these y/s locations. Inboard, the pressure distributions near the leading-edge indicate a transition bubble, in both the swept and unswept cases; thus it seems that here sweep does not result in a different transition mechanism. The pressure recovery associated with the standard configuration indicates the onset of stall near the trailing-edge, consistent with NACA 0015 airfoil data, [10] while that of the swept configuration is consistent with attached flow. Further outboard, this situation reverses (see figs. 5b and 5c and inset in fig. 5d showing the trailing-edge C_p) and the swept trailing-edge indicates the commencement of trailing-edge stall outboard. Tip stall on swept wings is generally attributed to both the higher loading at the tip and the thicker boundary layer that is driven outboard towards the tip by the transverse pressure gradient. For the present configuration, both mechanisms are active. In the former case, loading increases because the lift coefficient measured parallel to the flow direction tends to infinity as the chord-length tends to zero. In the latter case, a strong pressure gradient normal to

the flow direction is present as can be inferred by comparing C_p at $x/c=0.7$ and 0 in figs. 5a and 5c, which are both at the same distance downstream from the wing apex. It is believed that this is the dominant mechanism as trailing-edge separation, as inferred for the trailing-edge C_p , is observed as far inboard $y/s=0.3$. Note, however, that the distance from the apex of the triangular wedge is not accounted for in this coordinate system.

The relatively low pressure at the tip of the standard configuration also present for fully attached flow and is due to the vortex rollup, which is partially completed on the wingtip itself (cf. fig. 5d and fig B3a in appendix B). The structure of the tip vortex, and its response to control are discussed in section III.A.3 below. In contrast, there is a dramatic decrease in lift towards the tip for the swept configuration (see figs. 4b and 5d). Here the vortex forms outboard of the wing as observed by [9] as the wingtip edge is swept inboard. This unfavorable result emphasizes that the design of planform shapes such as this are motivated by factors other than aerodynamic performance.

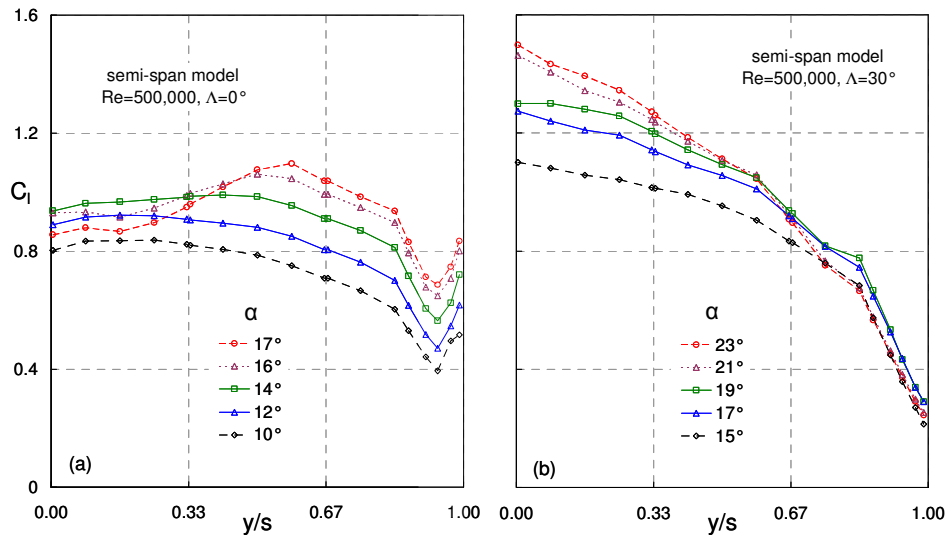


Fig. 4. Baseline span-load variations for (a) standard and (b) swept configurations based on integrated chordwise pressures on the rectangular section of the model corresponding to fig. 3. (No wingtip extensions.)

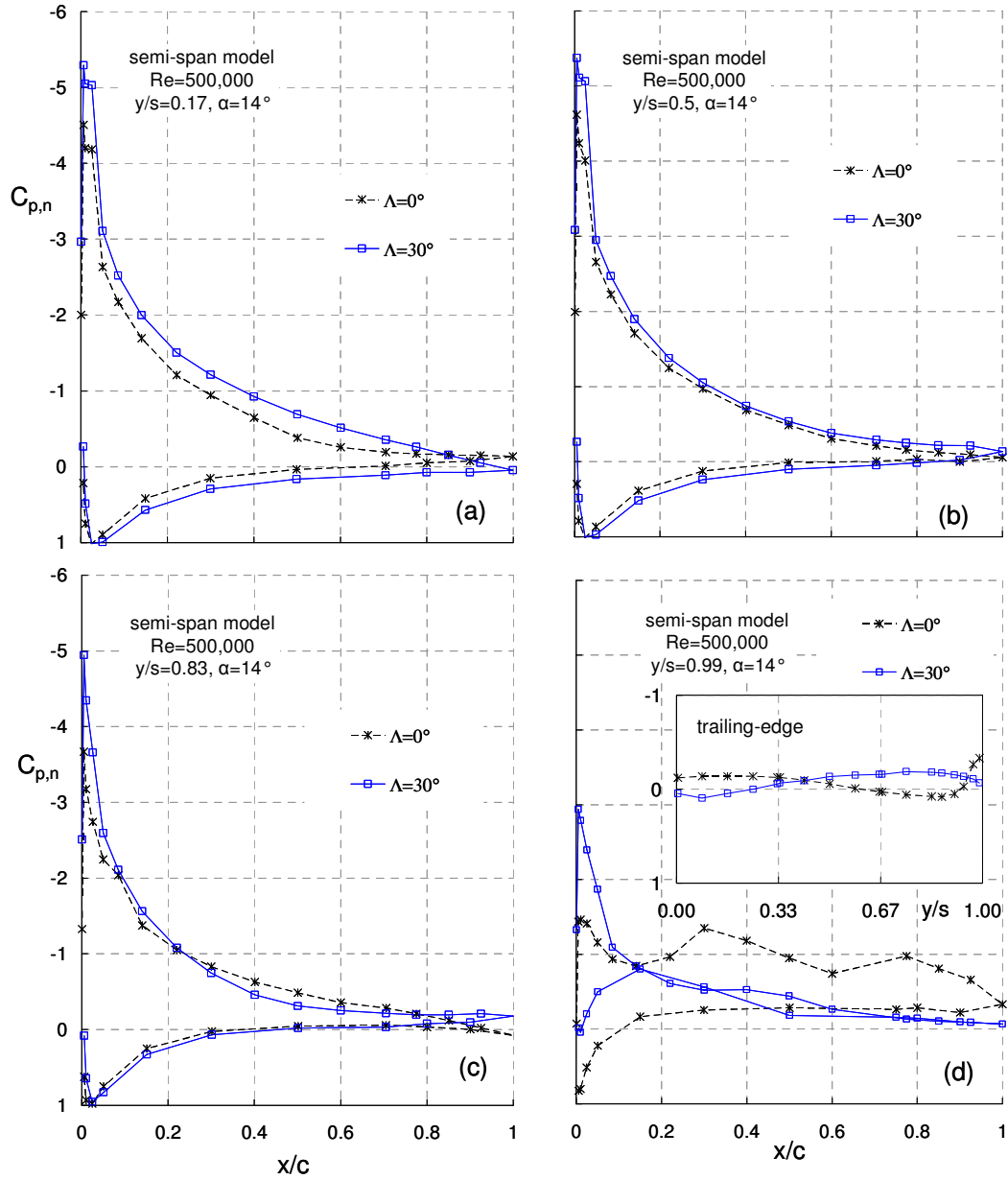


Fig. 5. Baseline pressure coefficient distributions at selected locations on the rectangular section of the model for standard and swept configurations (no wingtip extensions). Inset: corresponding trailing-edge pressure coefficients.

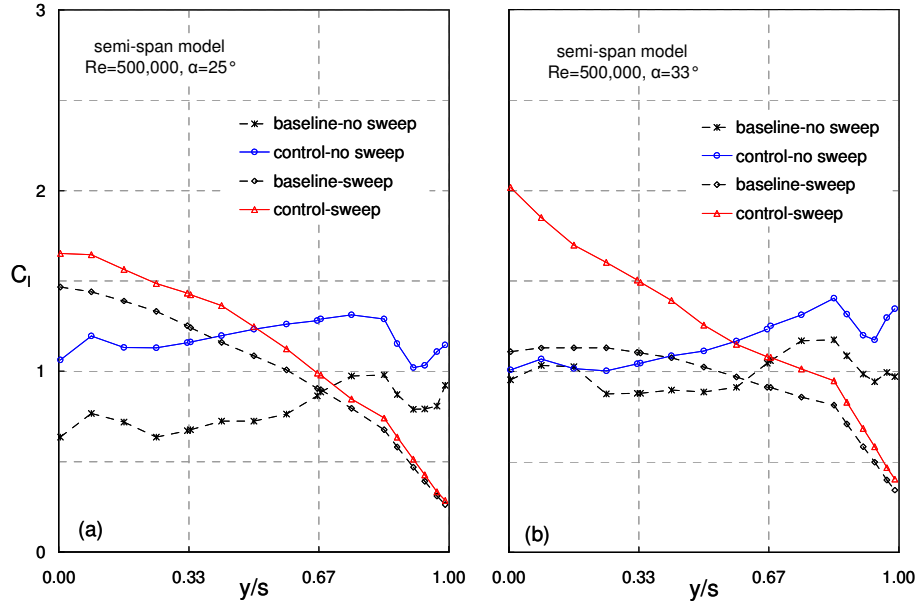


Fig. 6. Lift coefficient distributions, showing the effect of leading-edge control, at two angles of attack for both standard and swept configurations (no wingtip extension.) Control at $C_{\mu}=0.3\%$ and $F^+=0.65$.

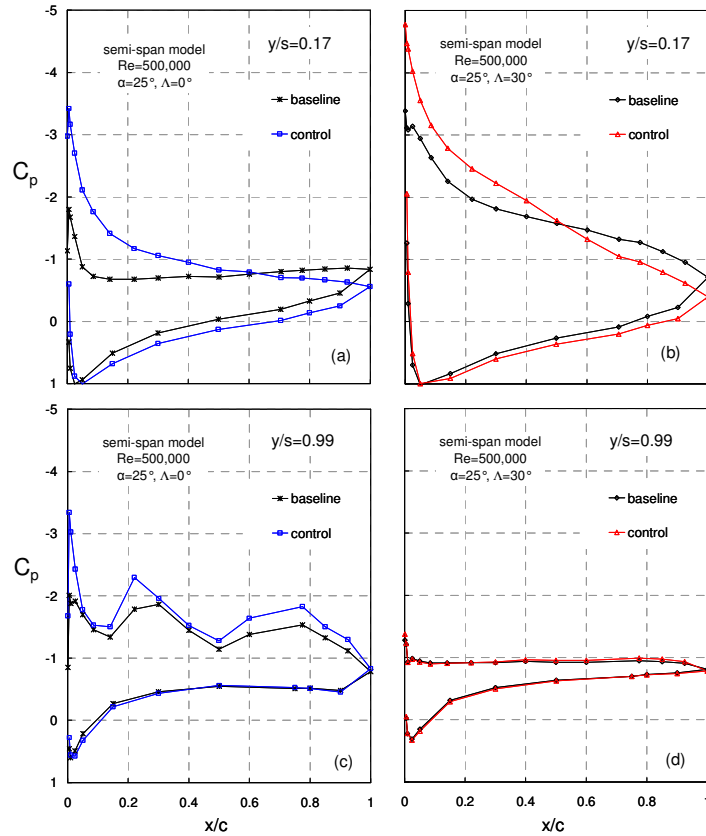


Fig. 7. Baseline and controlled pressure coefficient distributions at selected locations on the rectangular section of the model for standard and swept configurations ($\alpha=25^\circ$; no wingtip extension).

2. *Effect of Sweep on Leading-edge Control*

Figs. 6a and 6b show spanwise pressure distributions for two post-stall angles of attack ($\alpha=25^\circ$ and 33° respectively) for both configurations. At the lower angle, control is effective across the entire span for the standard configuration, but at the higher angle control is less effective inboard and only maintains some authority outboard in the tip region (cf. fig. 4a). With sweep, control is ineffective near the tip, irrespective of α . However, at high angles of attack control is particularly effective inboard with $\Delta C_l \approx 1$ near the root of the wing. Pressure distributions inboard ($y/s=0.17$) and at the tip ($y/s=0.99$) corresponding to these conditions for both configurations are shown in figs. 7a-7d and 8a-8d.

The largest improvements in performance are generally attained when the perturbations are introduced at, or close to, the separation line. Thus on sharp-edged delta wings this can be achieved by introducing perturbations at the leading-edge [22]. On the NACA 0015 tested here, this is clearly not the case as separation commences at the trailing-edge (figs. 5a and 5c) and then progresses upstream with increasing α (figs. 7a and 7b) and ultimately separates at the leading-edge (figs. 8a and 8b), consistent with previous observations [8]. On an equivalent unswept airfoil, control from an aft ($x/c=0.75$) slot was found to be more effective at angles just beyond the static stall angle [38]. However, the enhanced control ultimately promoted separation at the leading-edge. The combination of aft control over deflected flaps in conjunction with sweep is discussed fully in section III.B.

The swept-wing pressure distribution is significantly different to the unswept case at $\alpha=25^\circ$ and suggests the existence of vortical flow present at the leading-edge (fig. 7b and 7a), similar to that of a delta wing. Nevertheless, this is not a fully separated shear layer such as those typically occurring sharp-edge delta wings. When control is applied, the *effect* on the swept wing is similar to the *effect* on the unswept wing, i.e. the leading-edge suction peak is strengthened in both cases and so is the overall pressure recovery, leading to enhanced lift. We can thus conclude that the *control mechanism* is similar and we shall exploit this observation below in section III.A.4. When the wing enters into deep stall with leading-edge separation, as shown in figs 8a and 8b ($\alpha=33^\circ$), the effect of control is somewhat different. In both instances the suction peak is strengthened, but the effect on the unswept wing is mainly local near the leading-edge. In

contrast, for the swept wing a pressure recovery is reestablished and wing circulation is materially increased as can be inferred from the lower surface pressures. This latter case appears to have much in common with control of sharp-edged delta wings in which vortex breakdown has occurred. As observed previously, control regenerates the leading-edge flow thereby significantly enhancing lift [22]. There is no reason to believe that the vortex enhancement mechanism at $\alpha=25^\circ$ (fig. 7b) is any different to the vortex regeneration mechanism observed at $\alpha=33^\circ$ (fig. 8b). When viewed from this perspective, it is evident that the present study may aid in providing a link between unswept, swept and delta wing studies.

The effect of control on the tip flow is strikingly different. For the unswept tip, the existing tip vortex is somewhat strengthened at low α (fig. 7c) and significantly strengthened at and higher α corresponding to deep inboard stall. In contrast, virtually no effect is observed on the wingtip with sweep at any α (figs. 7d and 8d). These vastly different effects are discussed fully below in sections III.A.3 and III.A.4, respectively.

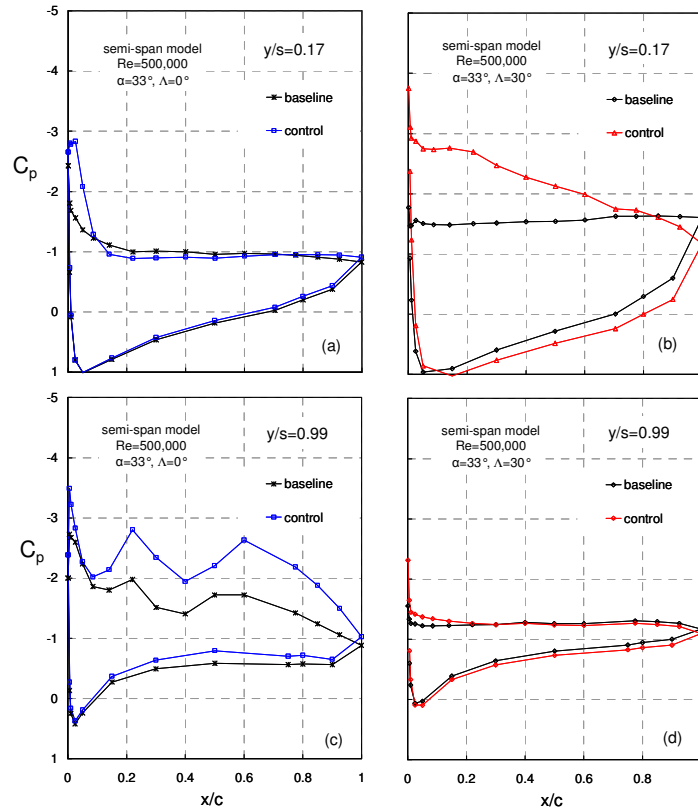


Fig. 8. Baseline and controlled pressure coefficient distributions at selected locations on the rectangular section of the model for standard and swept configurations ($\alpha=33^\circ$; no wingtip extension).

The addition of a parallel tip (see schematic in fig. 2c) has a beneficial effect on the baseline lift (fig. 9), and particularly the lift generated in the vicinity of the wingtip (figs. 10a and 10b). The parallel tip increases the wing aspect ratio, and this results in a general increase in lift noted across the entire wingspan. More significantly, the parallel tip renders the original outboard pressure ports further inboard and this is reflected as significantly increased lift near the tip. The parallel tip does not qualitatively change the stalling mechanism, as stall still commences outboard while inboard lift increases (not shown). Note, however, that the parallel tip was not instrumented with pressure ports, and hence the additional lift and form drag could not be estimated. Despite the enhanced baseline lift, improvements to control effectiveness, measured in terms ΔC_L for each case considered individually, is negligible (fig. 9). It is further evident from figs. 10a and 10b that the increment in C_l across the entire span resulting from control is virtually unchanged as a result of the parallel tip. It can therefore be concluded that the specific tip shape does not materially affect active control in the tip region.

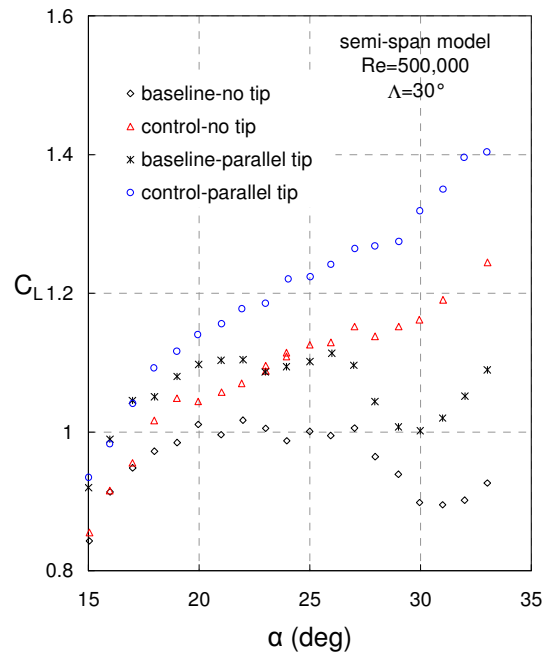


Fig. 9. Wing lift coefficient on the swept configuration, showing the effect of the parallel wingtip on leading-edge control effectiveness (control at $F^+=0.65$ and $C_\mu=0.3\%$).

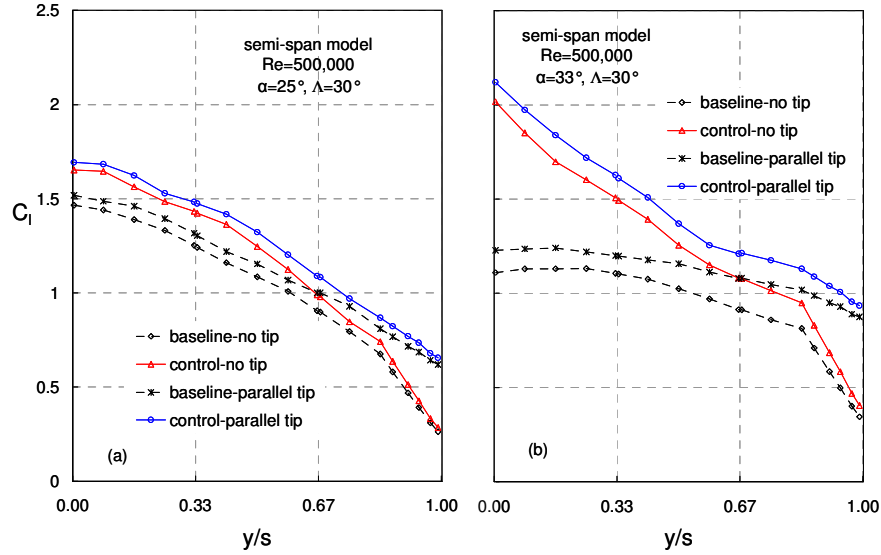


Fig. 10. Lift coefficient distributions on the swept configuration, showing the effect of the parallel wingtip on leading-edge control effectiveness (control at $F^+=0.65$ and $C_\mu=0.3\%$).

3. Control Mechanism on the Standard Configuration

The difficulty of developing a theoretical or computation model for the observations reported here cannot be overstated. For purely two-dimensional flows, with well-defined turbulent inflow conditions, unsteady computations using a variety of turbulence models can, at best, only describe qualitative time-mean trends [29]. The poor predictions are due the inherent flow complexity, where turbulence coexists with so-called coherent structures, which are usually driven by at least one instability mechanism. Consequently, there are no known models that can adequately calculate the effect of leading parameters such as reduced frequency and perturbation amplitude. For the unswept wing considered in this investigation, the flow is laminar or transitional in the vicinity of the leading-edge slot and also may be subjected to competing instability mechanisms due to curvature at the leading-edge region. The addition of sweep would further exacerbate existing difficulties due to the additional axial velocity component and the transverse pressure gradient that drives the boundary layer towards the tip.

A number of experimental investigations, motivated by rotorcraft blade tip optimization and trailing vortex problems, combine to yield a detailed representation of the vortex at the wingtip [9,10,11,12,30,31]. At conditions approaching stall ($\alpha=12^\circ$), a primary vortex rolls up on the upper surface adjacent to the tip, aft of which a counter-rotating secondary vortex is observed. This is consistent with flow visualization [30] and hot-wire measurements [31], and results in a

local increase in lift, represented by a pressure signature with three peaks (see figs. 5d, B3(a) and refs. [9] to [11]). However, the increased lift is accompanied a pressure drag penalty, due to the low-pressure peaks being aft of the profile maximum thickness point. The continuation of this triple pressure peak into the post-stall regime, as seen in figs. 7c and 8c, indicates that that the basic vortex structure does not change when the wing stalls inboard.

It was noted above that at larger post stall angles ($\alpha=33^\circ$; fig. 6b) control is more effective outboard towards the tip, in spite of the fact that the perturbation momentum is 40% lower than inboard (see fig. A2, in appendix A). Thus the tendency of flow to attach near the wingtip may be in some way related to the vortical wingtip flow discussed above. To illustrate this, consider the structure of the post-stall tip flowfield, in the presence of leading-edge perturbations, shown schematically in fig. 11 (adapted from [9]). In the region remote form the tip, or in a two-dimensional flow, separation is ameliorated by the control-driven quasi-two-dimensional spanwise vortices that transport momentum across the shear layer. Near the tip, momentum is transported by a combination of spanwise control-driven vortices and the primary vortical flow at the wingtip. This is a plausible explanation of why control is more effective near the tip at high angles of attack. The relatively smaller effect near the tip at lower angles of attack (e.g. fig. 6a) is because the flow is only mildly stalled in this region.

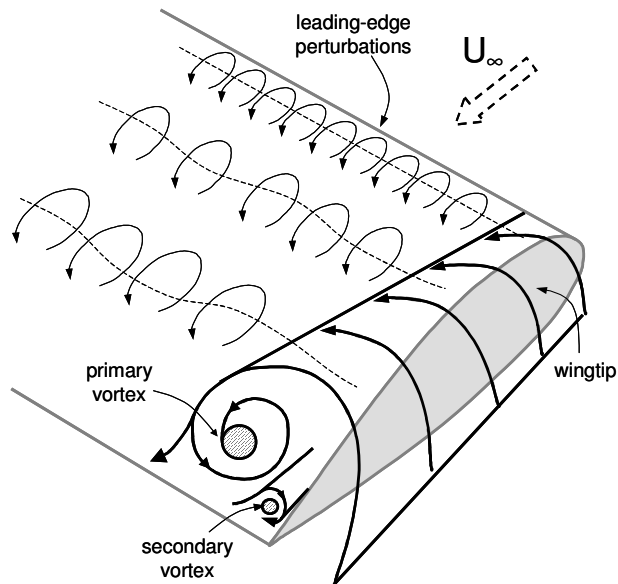


Fig. 11. Schematic of the tip vortex on a square-tipped wing in the post stall regime, where two dimensional separation control perturbations are generated at the leading-edge (adapted from [9]).

4. Sweep Relations Applied to Control

In considering control effectiveness on a swept airfoil that approximated infinite span [15], it was noted that performance benefits were similar to the unswept case providing that the flow normal to the wing was considered. In addition, based on the observations in III.A.2 above, the inboard effect of control is similar whether the wing is swept or not. Thus the re-circulating region that results from leading-edge control, in a time-mean sense, can also be expected to be present in the swept case. It should be expected, however, that the velocity component tangential to the leading-edge (axial velocity with respect to the vortex) has a stabilizing effect on the vortex.

To try and understand the effect of control in the presence of sweep, we assume that the control perturbations generated at the leading-edge are amplified and are convected downstream, normal to the leading-edge, much like their two-dimensional counterparts [32,33]. In the presence of sweep, however, there is a component of velocity tangential to the wing leading-edge, namely

$$U_{\infty,t} = U_{\infty} \sin A' . \quad (6)$$

Therefore the evolving perturbation will have a chordwise as well as a spanwise component.

Empirical data, on a NACA 0015 airfoil, of the fundamental perturbation (fig. 12; ref 11) shows that the phase velocity can be quantified to first approximation by the relationship:

$$U_{\phi} / U_{\infty} = k(x/c)^r \quad (7)$$

where k and r are constants that depend upon the separation control reduced frequency F^+ (see fig. 12). Moreover, the perturbation phase velocity is only weakly dependent on the perturbation amplitude (cf. [32] and [33]). Thus, to a first approximation, we assume that a similar relationship holds for flow normal to the swept wing, namely:

$$U_{\phi,n} / U_{\infty,n} = k(x/c)^r \quad (8)$$

where k and r now depend on the reduced frequency F^+ defined normal to the leading-edge, F_n^+ (see eqn. 5).

From equations (2), (6) and (8), the speed of the perturbation can be expressed as

$$U_{\phi} / U_{\infty} = \sqrt{k^2 (x/c)^{2r} \cos^2 A' + \sin^2 A'} \quad (9)$$

and its trajectory or “streamline” angle can be expressed as:

$$\varepsilon_\phi = \sqrt{\tan \Lambda' / k(x/c)^r} \quad (10)$$

At $F^+=1.1$ it is seen that that perturbation speed is greater close to the leading-edge, but slows further downstream and even decreases slightly. The effect of this on the analysis presented above is discussed below.

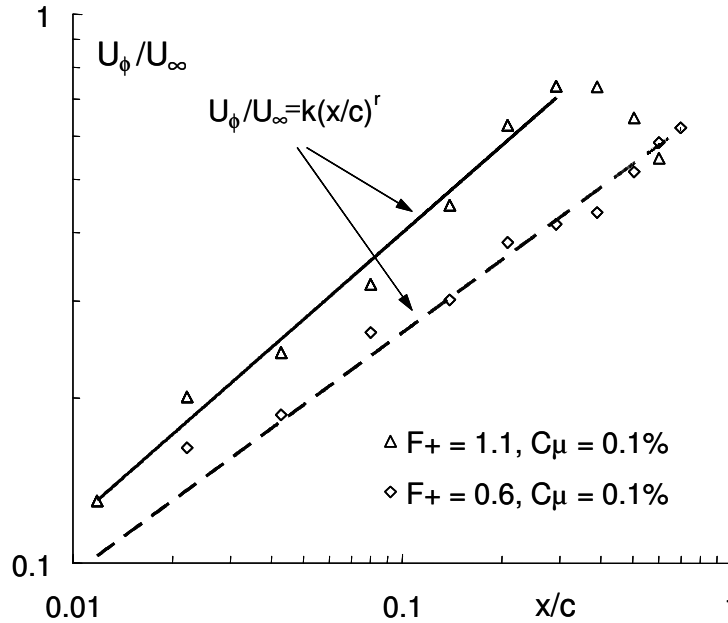


Fig. 12. Fundamental components of the phase-velocity measured on a NACA 0015 airfoil. [32]

By using empirical airfoil data to determine constants k and r at the control conditions $F^+ = 0.6$ and $C_\mu=0.1\%$ (fig. 12), trajectories for different sweep angles were calculated (see fig. 13). The figure shows how the perturbation trajectories are swept across the span as a result of the tangential velocity component. Thus perturbations introduced near the tip will be swept off the wing without producing any meaningful change to the aerodynamic loads. Furthermore, as the sweep angle increases, the tangential velocity component increases and the effect is expected to diminish even more.

The above description provides a basic explanation for the gradually decreasing effect of control along the span and its total ineffectiveness at the tip. It can be seen from fig. 12 that, at $F^+=1.1$, the approximation expressed in eqn. 7 breaks down at $x/c \approx 0.3$. At larger x/c the phase velocity tends towards a constant value, typically around $U_\phi/U_\infty = 0.5$ to 0.6 . Taking this into, results in

the perturbation trajectory being deflected toward the tip to an even greater degree. This scenario is indicated by the hatched line, associated with the $\Lambda'=30^\circ$ case, shown in fig. 12 and shows that the assumption of eqn. 7 in fact underestimates the deleterious effects of sweep on tip flow separation control at higher F^+ .

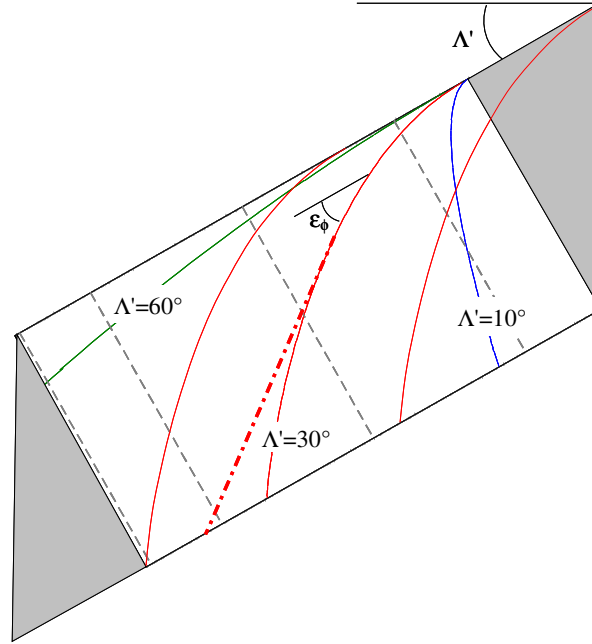


Fig. 13. Semi-empirical prediction of the fundamental component of the phase-velocity on a swept NACA 0015 wing based on data from fig. 12 ($F^+=0.65$ and $C_\mu=0.1\%$). The hatched line indicates constant $U_{\phi n}$.

5. Effect of Varying Free-Stream Velocity

The attachment or separation of a shear layer to or from a vehicle wing is generally accompanied by a change in vehicle speed. In the former case, initiating active flow on a stalled wing, will generally increase lift, reduce drag and thereby result in acceleration of the vehicle. In the latter case, for example a sharp change to in attack on a controlled wing, with accompanying increase in drag, will result in a deceleration of the vehicle. Quasi-steady simulations of speed changes were simulated in the wind tunnel by changing the tunnel flow speed (U_∞), corresponding to the range $10^5 \leq Re \leq 10^6$, for standard and swept configurations at a large post-stall angle of attack, $\alpha=33^\circ$. Control was applied at $f=55\text{Hz}$ and $U_p=17\text{m/s}$ (47.6Hz and 15m/s for the swept case), in order to maintain the reduced frequency within the range considered to be effective ($0.3 \leq F^+ \leq 2.6$) and the perturbation amplitude corresponded to $0.02\% \leq C_\mu \leq 2\%$. The physical frequencies and

amplitudes are cited here because the dimensionless frequency and momentum coefficient are not constant, and vary with $1/U_\infty$ and $1/U_\infty^2$ respectively.

Lift and moment coefficient data is shown for standard baseline and control cases, where the flow speed, or Reynolds number, is initially decreased from $Re=10^6$ to 10^5 and subsequently increased to $Re=10^6$ (figs. 14a and 14b show outboard, $y/s=0.83$, and overall wing lift and moment coefficients). Two data points were acquired at each Re based on a 15s average for each data point. The baseline data exhibits significant hysteresis, in that the flow state is dependent on whether U_∞ is increasing or decreasing. Moreover, the flow is typified by bi-stable flow states, i.e. either partially attached or fully separated, where these states can either occur spontaneously without any apparent reason, or they can be induced by small changes in U_∞ . The net result is relatively large and spontaneous variations in aerodynamic loads, which are highly undesirable. Despite the order of magnitude variation in dimensionless conditions, particularly F^+ , control eliminates the bi-stable characteristic and consequently also eliminates hysteresis as a function of Re . These observations have been made before in the context of constant U_∞ , but not for conditions of varying U_∞ as presented here. Form drag exhibited similar behavior where L/D was typically between 1.3 and 2.

The identical exercise to that described above was performed on the swept configuration (figs. 15a and 15b show inboard, $y/s=0.83$, and overall wing lift and moment coefficients). With the introduction of sweep, the bi-stable flow associated with changing velocity in the baseline case is eliminated and the coefficients are virtually independent of the changing velocity. This difference between the post-stall baseline flows of the two configurations is consistent with the C_L versus α data shown in figs. 3a and 3b. With control, the stable character is maintained and lift is enhanced, particularly inboard (fig. 15a). In addition, despite the relatively large increases in C_μ at low velocities, maximum inboard lift enhancement is achieved at $F^+\approx 0.6$; this is consistent with the present unswept data as well as airfoil studies [1,8,33].

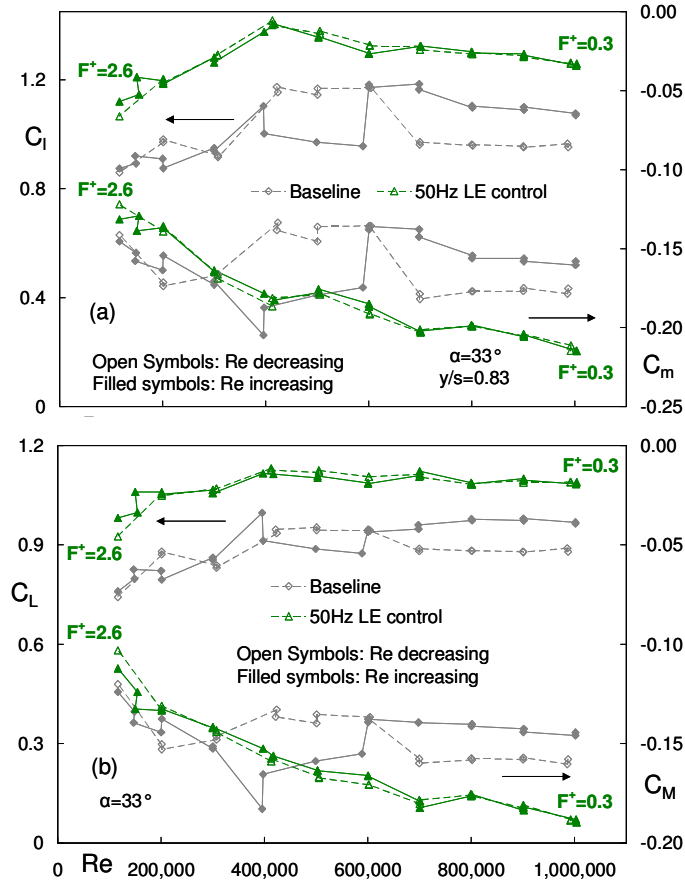


Fig. 14. Effect of changing free-stream velocity on the baseline and controlled standard model lift and moment coefficients (a) near the wingtip and (b) of the wing. Control at a constant frequency of 50Hz and $U_p=17\text{m/s}$.

The favorable response of the flow to a range of reduced frequencies, rather than a single reduced frequency, was exploited here by selecting the physical control frequency *a priori* to produce $0.3 \leq F^+ \leq 2.6$. Thus, providing that the minimum threshold perturbation amplitude is exceeded, a fixed frequency can be used to effect control for a range of Reynolds numbers varying approximately by one order of magnitude. The effectiveness of control near the unswept wingtip does not diminish between $\alpha=25^\circ$ and 33° (cf. figs. 6a and 6b). A similar conclusion can be drawn with respect to inboard control on the swept configuration, which in fact becomes more effective at higher α . It is therefore reasonable to assume that control effectiveness in the standard configuration tip and swept inboard regions will be effective to even higher angles of attack, although this could not be verified due to limitations associated with the experimental setup.

The effectiveness of control near the tip, but not inboard, on the standard configuration is mostly due to enhancement of the tip vortex strength. On the other hand, effectiveness of control inboard with sweep is presumed to be due to the generation and stabilization of the leading-edge vortex by the tangential (vortex-axial) flow. Nevertheless, based on the above discussion, we conclude that leading-edge active flow control at a single frequency can in principle be employed for vehicle control at very high α and at a range of speeds. One possible application may be to alleviate buffet and hysteresis on tilt-wing aircraft during the critical transition from vertical to horizontal flight as well a managing the so-called “barn door effect” during hover [34,35]. The maximum lift observed in fig. 15 corresponds to the range $0.45 \leq F^+ \leq 0.65$, as defined for the swept wing in section II.B. It is therefore concluded that sweep does not have meaningful effect on the optimum control frequency, but it does affect the nature of control dramatically.

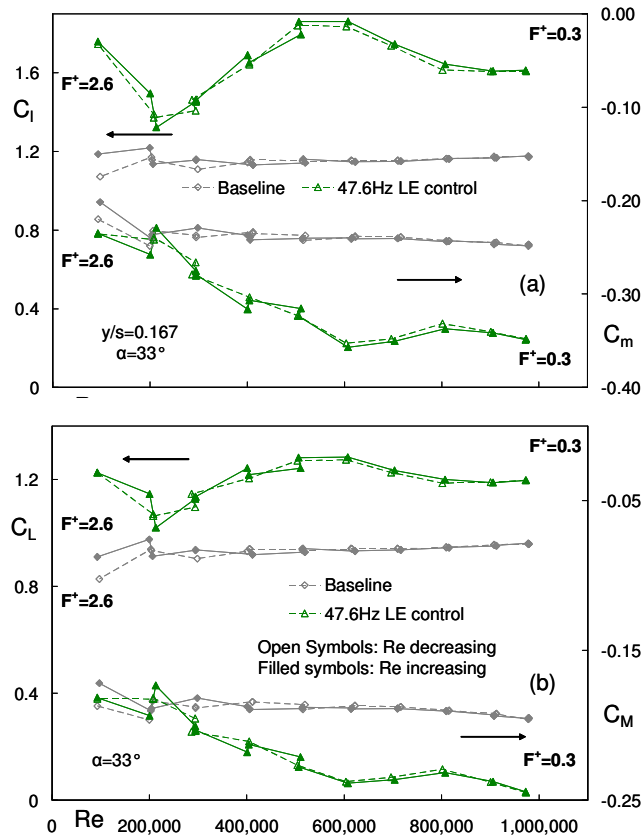


Fig. 15. Effect of changing free-stream velocity on baseline and controlled swept model lift and moment coefficients (a) inboard and (b) of the wing. Control at a constant frequency of 47.6Hz and $U_p = 15\text{m/s}$.

6. Leading-edge Control with Flap Deflection

Data for $\delta=(20^\circ,20^\circ,20^\circ)$ and $\delta=(40^\circ,40^\circ,40^\circ)$ flap deflections are presented in figs. 16a and 16b, where control is supplied from the leading-edge. For all leading-edge control data on the swept wing, the gap between the inboard edge of the inboard flap and the wind tunnel wall was sealed. At 20° flap deflection, the flow over the flap appears to be partially attached up to $\alpha \approx 1^\circ$ for both swept and unswept configurations; at 40° flap deflection the flap is stalled throughout the range of α considered here. Table 2 shows the changes to $\Delta C_{L,max}$ as a result of leading-edge control combined with flap deflection. In both standard and swept configurations, $\Delta C_{L,max}$ diminished as a result of increasing flap deflections, although clearly $C_{L,max}$ increases. Thus flap deflection has a mild deleterious effect on leading-edge control effectiveness. Nevertheless, in a similar fashion to the symmetric wing case (no flap deflection), the majority of the lift enhancement is in the vicinity of the wing root while lift enhancement near the tip is negligible (figs. 17a and 17b) and the chordwise pressure distributions are similar (not shown).

Table 2. Changes in maximum lift coefficient ($\Delta C_{L,max}$) resulting from a combination of leading-edge control and flap deflections.

$(\delta_i, \delta_o, \delta_t)$	standard	Swept	tip configuration
$(0^\circ, 0^\circ, 0^\circ)$	~ 0.24	> 0.23	no extension
$(20^\circ, 20^\circ, 20^\circ)$	~ 0.12	~ 0.20	no extension
$(40^\circ, 40^\circ, 40^\circ)$	~ 0.10	~ 0.13	no extension

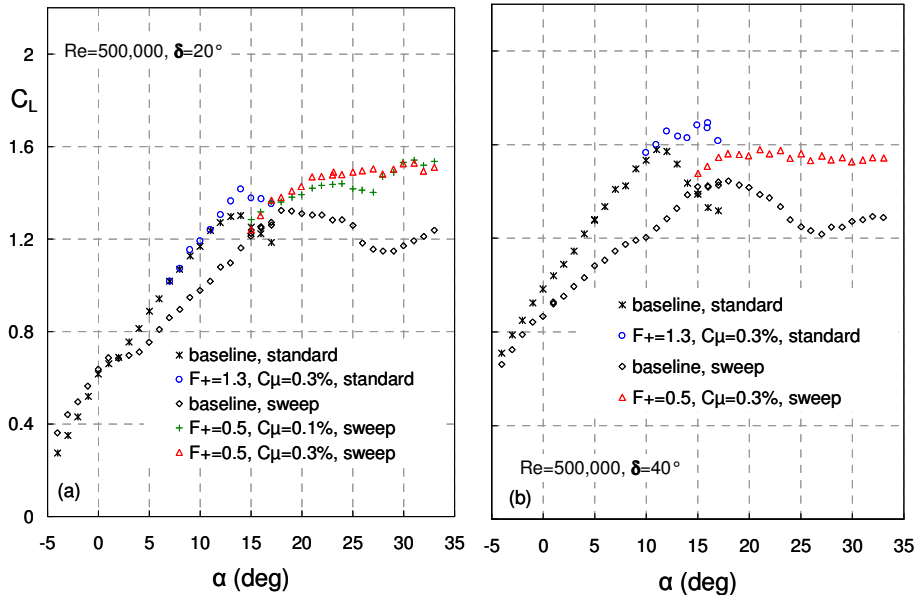


Fig. 16. The effect of control from the leading-edge in the presence of flap deflection (a) $\delta=(20^\circ,20^\circ,20^\circ)$ and (b) $\delta=(40^\circ,40^\circ,40^\circ)$.

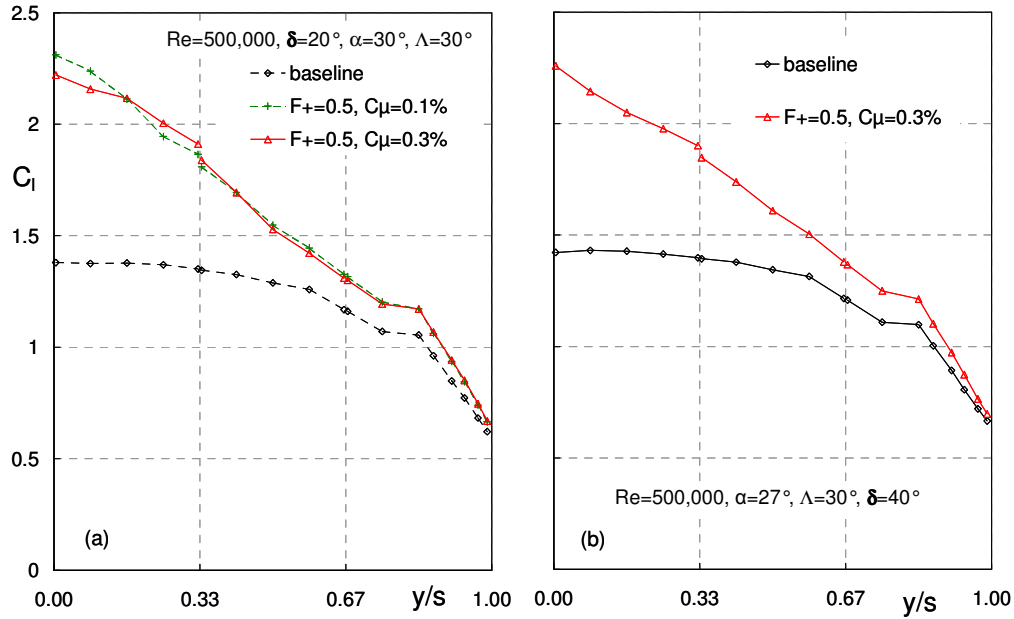


Fig. 17. Spanwise load variation for leading-edge control in the presence of flap deflection (a) $\delta=(20^\circ,20^\circ,20^\circ)$ and (b) $\delta=(40^\circ,40^\circ,40^\circ)$.

B. Control from the Flap-shoulder

1. Finite Flap Length

The effect of control in the presence of a finite flap span was assessed by comparing control on individually deflected flaps with control over the entire wingspan, $\delta=(20^\circ,20^\circ,20^\circ)$. The specific flap deflections considered were: (i) inboard and outboard flaps simultaneously $\delta=(20^\circ,20^\circ,0^\circ)$; (ii) the inboard flap $\delta=(20^\circ,0^\circ,0^\circ)$; and (iii) the outboard flap $\delta=(0^\circ,20^\circ,0^\circ)$; figs. 18a-18h. Tip-flap deflection alone was not considered here. In the above figures depicting the span-load variation (C_l vs. y/s), data set pairs depict baseline and control cases respectively; in all cases the wingtip extension was not installed (cf. fig. 1a). All controlled flows were subjected to the same control perturbation frequencies and amplitudes along the span in order to facilitate an objective comparison between the various cases. It is evident from the data that control is effective across the span of each deflected flap. This can clearly be seen by comparing the C_l near the flap edge and the adjacent un-deflected flaps for baseline and control cases $y/s=0.33$ and/or 0.67 in figs. 18c-18h). This has a significant effect on the flap trailing vortex properties as discussed in detail in refs. [36] and [37].

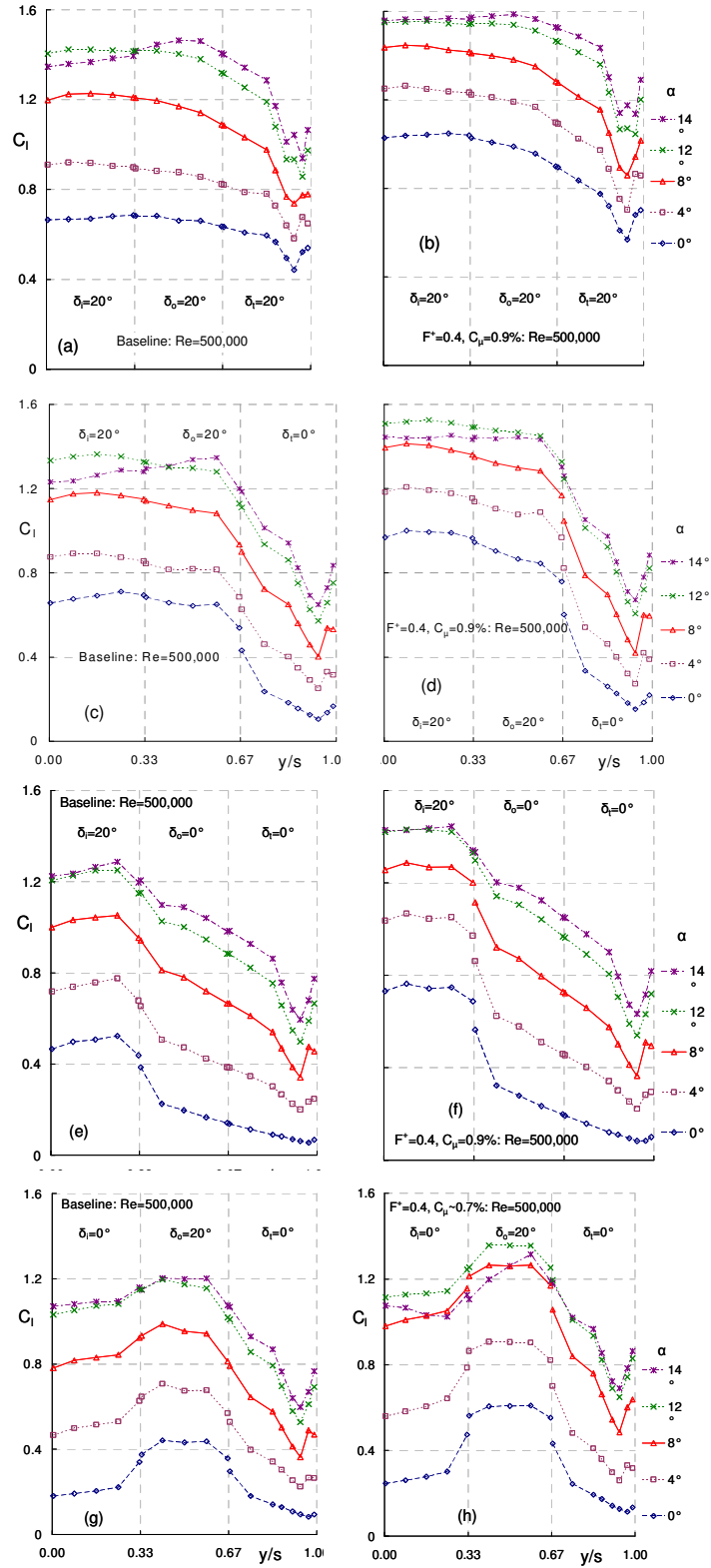


Fig. 18. Spanwise load variation showing the effect of control for different flap deflections, (a-b): full span; (c-d): inboard and outboard; (e-f): inboard; (g-h) outboard.

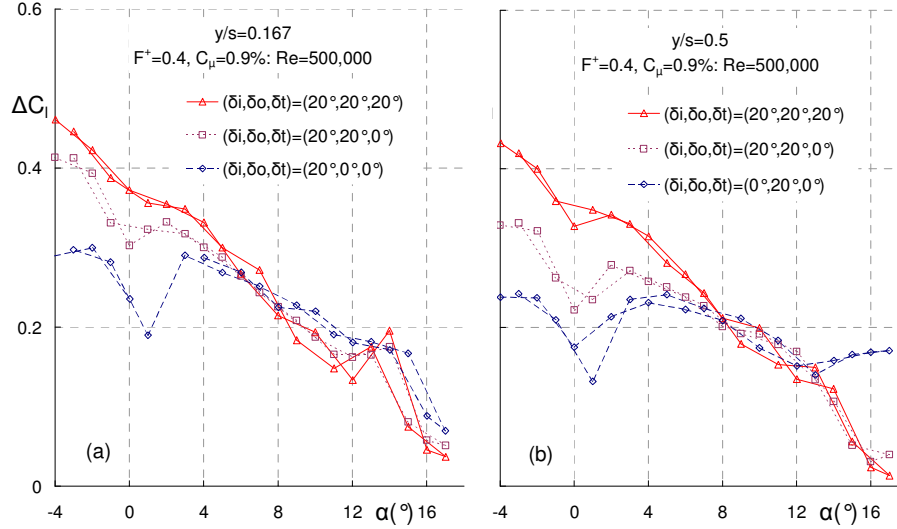


Fig. 19. Lift coefficient change with angle of attack (a) inboard and (b) at the midspan for different flap deflections.

Successively shorter flap-span deflection, (i) to (iii) above, produces a successively narrower spanwise separated zone. The effect of this on control effectiveness is shown in fig. 19a where the local inboard ($y/s=0.167$) C_l is plotted as a function of α . At angles of attack less than 4° , the lift enhancement is greatest when all flaps are deflected and the effectiveness diminishes with successively narrower separated region. However for angles greater than approximately 6° the differences in lift enhancement are small, and at α_{\max} there is a small but measurable switchover, with the shorter flap span producing more lift enhancement locally. This is believed to be due to enhancement of the flap-edge vortices, in direct analogy wingtip enhancement described in section III.A.3. Similar observations are made with respect to the outboard flap lift ($y/s=0.5$, fig. 19b), with the exception that control is clearly more effective on the deflected outboard flap $\delta=(0^\circ, 20^\circ, 0^\circ)$ at angles of attack exceeding approximately 12° .

A further effect of the narrower spanwise separated zone concerns control effectiveness along the flap span. In figs. 20a and 20b the differences at the flap-edges are compared with those at the center span of the flap. At low angles of attack ($\alpha \leq 2^\circ$) the effect of control is comparable between the flap centerline and edges; however, higher C_l is generated at the outboard edge of the outboard flap for larger angles of attack. Inboard the differences are small with perhaps slightly larger lift enhancement near the wing/tunnel-wall junction (fig. 20b).

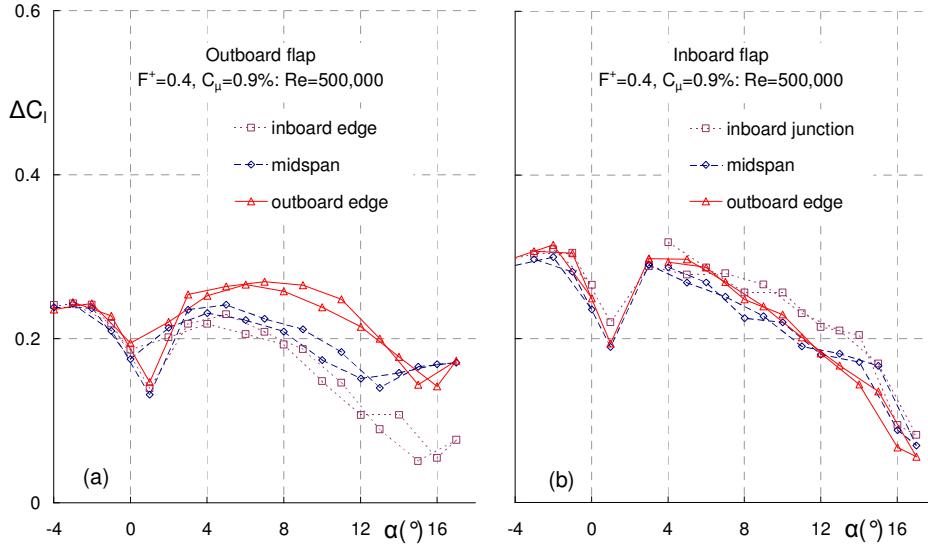


Fig. 20. Lift coefficient change with angle of attack at flap midspan and edges for the (a) outboard and (b) inboard flaps.

2. Flap-shoulder control with Sweep

Data for control from the flap-shoulder are shown for both standard and swept configurations in figs. 21-23. For all data presented, flaps are deflected in unison, i.e. either $\delta=(20^\circ,20^\circ,20^\circ)$ or $\delta=(40^\circ,40^\circ,40^\circ)$. The incremental changes to C_L associated with the standard configuration at 20° flap deflection are not matched by those of the swept configuration (fig. 21a). In addition, the increase in $C_{L,max}$ associated with the standard configuration is not matched by that of the swept configuration. At angles of attack greater than where the flap stalls ($\alpha > 1^\circ$) pressure coefficient distributions on the flap show slightly better recovery when sweep is introduced (e.g. figs. 22b-22c). This suggests that the flow on baseline swept configuration is less separated than that on the standard configuration. The reason for this is not clear, but it may be due to a stabilized vortical flow, resulting from the tangential velocity component at the flap-shoulder, and positioned over the flap. The pressure coefficients are based on the normal $U_{\infty,n}$ and the apparent enhanced attachment does not translate to higher lift. Much like in the case of leading-edge control, flap-shoulder control appears to be more effective inboard for the swept configuration, while control effects near the tip are negligible; this is evident from the span-load variations (figs. 23a). Unlike the case of leading-edge control, flap-shoulder control on the swept configuration does not produce larger increments inboard. As noted above, without sweep the effect of control is approximately uniform across the span (fig. 23a) and inboard its effect is

approximately double that of the swept configuration. At present there is no clear explanation why sweep has such a deleterious effect on flap-shoulder control.

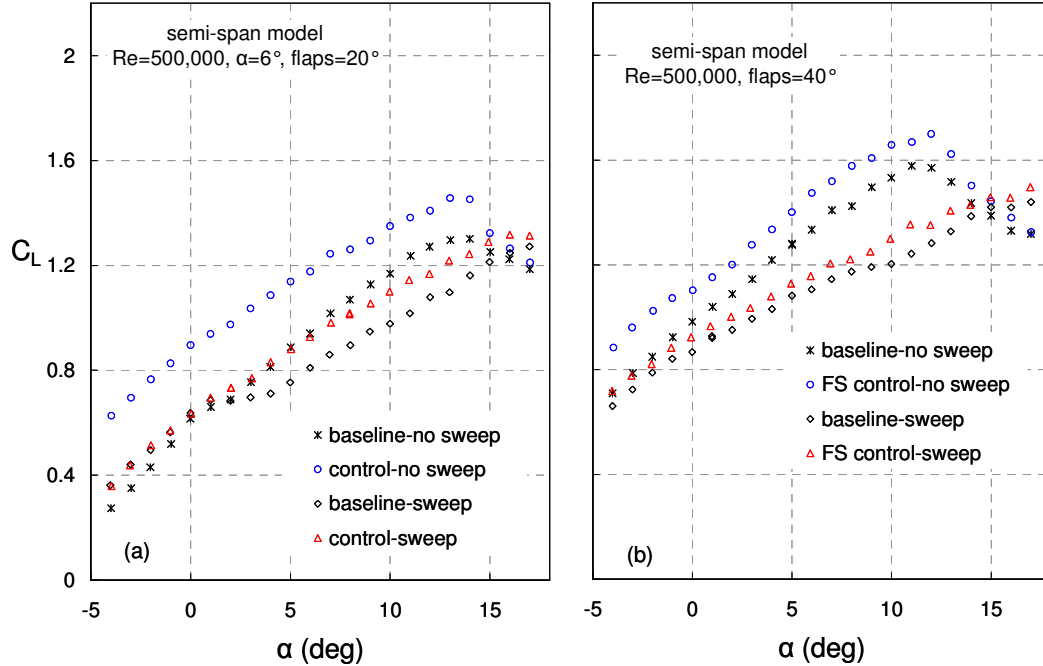


Fig. 21. Lift coefficient variation showing the effect of sweep on flap-shoulder control for (a) $\delta=(20^\circ,20^\circ,20^\circ)$ and (b) $\delta=(40^\circ,40^\circ,40^\circ)$. All control at $F^+=0.4$ and $C_\mu=1.4\%$.

At the large 40° flap deflection the control amplitude is not large enough to significantly control the flap flow for either the standard or swept configurations. Nevertheless, the standard configuration is once again more receptive to control, with a relatively small but uniform lift enhancement across the span. When sweep is introduced, almost no effect is detectable at $y/s>0.3$. Similar results to this above were observed with individual flap deflections, such as those presented in section III.B.1 (not shown). It can therefore be concluded that flap-shoulder control on low aspect ratio wings with substantial sweep (i.e. $\geq 30^\circ$), will not produce significant performance increments.

Figs. 24a and 24b simultaneously consider the effect of (i) the wingtip extension and (ii) the gap between the inboard edge of the inboard flap and the wind tunnel wall on the baseline flow. In the first case the flap-edge/wind-tunnel wall gap is left open and the wing is equipped with a square tip; in the second case this gap is sealed and no tip extension is present. The distance between the inboard and tip, and hence their negligible effect on one another, allows these

effects to be studied simultaneously. For both baseline cases the flap stalls at $\alpha \approx 1^\circ$ but the case with the gap flow produced slightly more lift. The gap assists in promoting attachment of the flow to the flap and this can be seen by the larger inboard lift (fig. 24b). With control the lift is slightly higher, but the difference between this and the baseline case is smaller than the baseline versus control difference associated with the sealed case. The lift near the tip drops dramatically irrespective of the whether there is a tip extension or not. However, inclusion of the tip does result in slightly higher lift in that region and the control effectiveness is also marginally better.

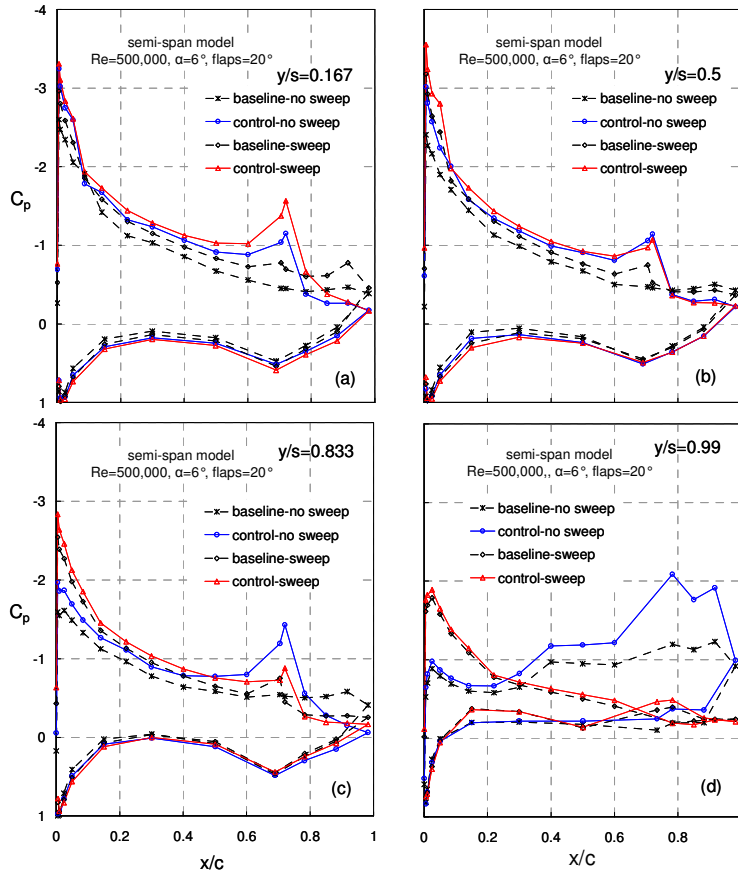


Fig. 22. Selected wing pressure coefficients showing the effect of sweep on flap-shoulder control at $\delta=(20^\circ, 20^\circ, 20^\circ)$. All control at $F^+=0.4$ and $C_\mu=1.4\%$.

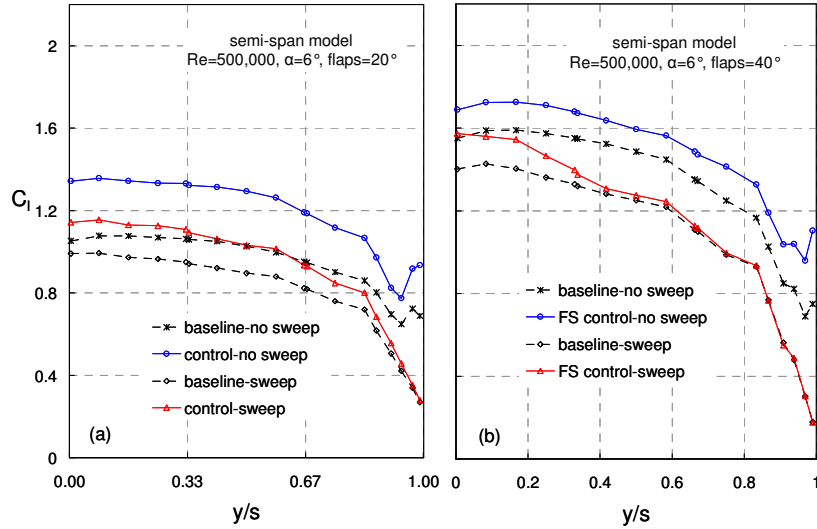


Fig. 23. Local lift variation showing the effect of sweep on flap-shoulder control for (a) $\delta=(20^\circ,20^\circ,20^\circ)$ and (b) $\delta=(40^\circ,40^\circ,40^\circ)$. All control at $F^+=0.4$ and $C_\mu=1.4\%$.

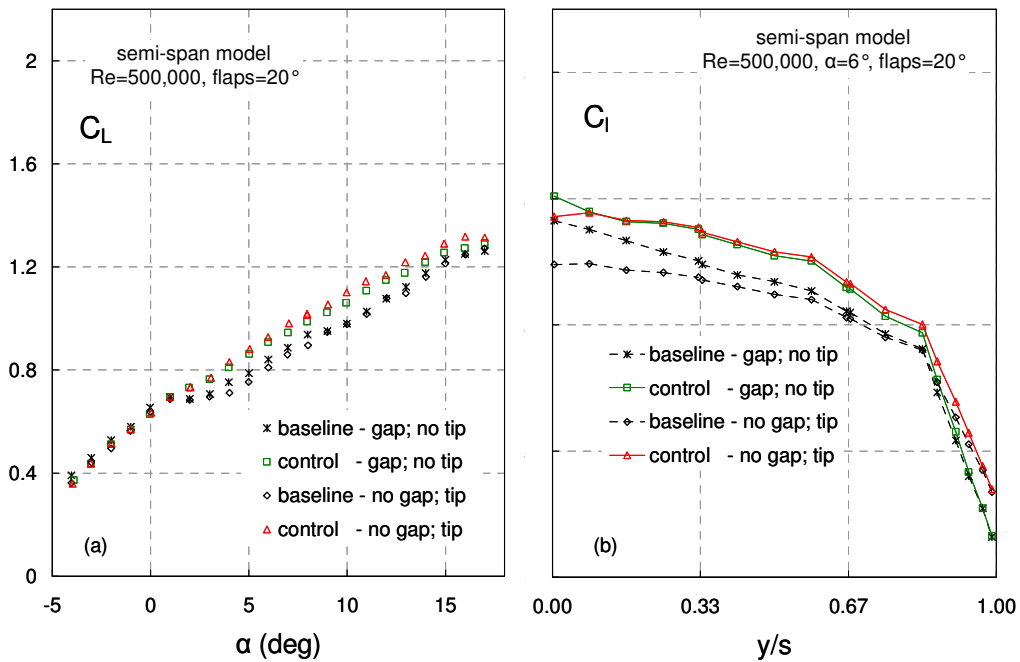


Fig. 24. Lift coefficient variation showing the effect of sweep on flap-shoulder control in the presence of a wing/tunnel-wall gap and with a wingtip extension at $\delta=(20^\circ,20^\circ,20^\circ)$. All control at $F^+=0.4$ and $C_\mu=1.4\%$.

IV. Summary of Main Findings

The efficacy of separation control on the semispan wing was investigated by means of leading-edge and flap-shoulder zero mass-flux blowing slots. Without sweep baseline stall was initiated inboard, but with sweep stall was initiated near the tip. In all instances, leading-edge perturbations were effective for increasing $C_{L,max}$ and post stall lift. Without sweep, the effect of control was approximately uniform across the wing span, but greater control authority was maintained near the tip at high α . With the introduction of sweep, a significant effect was noted inboard, but this effect degraded along the span and produced virtually no meaningful lift enhancement near the tip, irrespective of the tip configuration. These basic trends were maintained in the presence of flap deflections of 20° and 40°. In the absence of sweep, control on finite-span flaps did not differ significantly from their two-dimensional counterparts.

Based on this investigation and previous studies, it was concluded that control authority on the unswept wing was enhanced near the wingtip due to a combination of spanwise control-driven vortices and the primary wingtip vortex. Both of these served to transfer momentum to the upper surface, particularly at high post-stall angles of attack. This also sufficed to explain similar observations that were made when control was applied on finite span flaps at high angles of attack. Despite the different stalling mechanisms, it was noted that the qualitative effect of control on the inboard pressure distributions were similar with or without sweep at moderate post stall angles. This observation was used, in conjunction with empirical data from previous investigations, to develop a simple model, based on the trajectory or “streamline” of the perturbation. The empirical model served to explain the poor performance of separation control near the wingtip in the presence of sweep, irrespective of the tip configuration. The deep stall case, with leading-edge separation, had much in common with control of sharp-edged delta wings in which vortex breakdown has occurred. Here perturbations regenerated a vortical flow at the leading-edge, thereby significantly enhancing lift. It was thus asserted that the present investigation provides a link between unswept, swept and delta wing studies.

From an applications perspective, a case can be made for applying leading-edge control to wings with moderate sweep and/or high aspect ratio. However, flap-shoulder control on a swept wing

should not be expected to produce effects comparable to those on unswept configurations. Further work should aim at studying the effect of slot location, frequency and amplitude. Perhaps internally mounted actuators, such as those used in [39], can ameliorate the problems associated with perturbation two-dimensionality. Although it appears that the optimum reduced frequency is not materially affected by sweep, this should be studied for different sweep angles and reduced frequencies.

Acknowledgements

This work was performed while the first author held a National Research Council–NASA Langley Research Center Associateship. The authors wish to thank W. L. Sellers III for initially suggesting and supporting the study of basic three-dimensional effects in the context of active flow control. The authors also wish to thank S. A. Gorton, C. S. Yao, L. P. Melton, L. N. Jenkins, I. Wagnanski (University of Arizona) and H. Nagib (Illinois Institute of Technology) for their active assistance and many fruitful discussions; as well as R. D. White, A. Barnes and J. Harris for their exceptional technical support.

References

1. Greenblatt, D. and Wygnanski, I., "Control of separation by periodic excitation," *Progress in Aerospace Sciences*, Volume 37, Issue 7, pp. 487-545, 2000.
2. Greenblatt, D., "Dual Location Separation Control on a Semispan Wing," *AIAA Journal*, Vol. 45, No. 8, 2007, pp. 1848-1860.
3. Schlichting, H. 'Boundary Layer Theory,' McGraw-Hill, 7ed, 1979.
4. Amitay, M., Washburn A. E., Anders, S. G. and Parekh, D. E., "Active Flow Control on the Stingray Uninhabited Air Vehicle: Transient Behavior," *AIAA Journal*, Vol. 42, No. 11, 2004, pp. 2205-2215.
5. Chang, P. K., "Control of Separation", McGraw-Hill, New York, 1976.
6. McCroskey, W. J., McAlister, K. W., Carr, L. W. and Pucci, S. L., "An experimental study of dynamic stall on advanced airfoil sections", NASA TM-84254, July 1982.
7. Currier, J. M. and Fung, K. -Y., "Analysis of the Onset of Dynamic Stall", *AIAA Journal*, Vol. 30, No. 10, 1992, pp. 2469-2477.
8. Greenblatt, D. and Wygnanski, I., "Effect of leading-edge curvature on airfoil separation control," *AIAA Journal of Aircraft*, Vol. 40, No. 3, 2002, pp. 473-481.
9. Spivey, R. F., "Blade Tip Aerodynamics – Profile and Planform Effects," 24th Annual National Forum Proceedings of the American Helicopter Society, Washington, D.C., 1968.
10. McAlister, K. W. and Takahashi, R. K. "NASA 0015 wing pressure and trailing vortex measurements" NASA TP 3151 (AVSCOM Technical Report 91-A-003), November 1991.
11. Spivey, W. A. and Morehouse, G. G., "New insights into the design of swept-tip rotor blades," 26th National Annual Forum Proceedings of the American Helicopter Society, Washington, D.C., 1970.
12. Piziali, R. A., "2-D and 3-D oscillating wing aerodynamics for a range of angles of attack including stall", NASA TM 4632, 1994.
13. Dagenhart, J.R. and Saric W.S., "Crossflow Stability and Transition Experiments in Swept-Wing Flow," NASA/TP-1999-209344, 1999.
14. Nickel, K. and Wohlfahrt, M., "Tailless Aircraft in Theory and Practice," American Institute of Aeronautics Education Series, September, 1994.
15. Naveh, T., Seifert, A., Tumin, A. and Wygnanski, I., "Sweep effect on parameters governing control of separation by periodic excitation", *AIAA Journal*, Vol. 35, No. 3, 1998, pp. 510-512.
16. Seifert, A. and Pack, L.G., "Effects of Sweep on Active Separation Control at High Reynolds Numbers," *Journal of Aircraft*, Vol. 40, No. 1, pp. 120-126, 2003.
17. Rossow, V. J., "Lift enhancement by an externally trapped vortex," *AIAA Journal of Aircraft*, Vol. 15, 1978, pp. 618-625.
18. Saffman P. G. and Sheffield, J. S., "Flow over a wing with an attached free vortex," *Studies in Applied Mathematics*, Vol. 57, 1977, pp. 107-117.
19. Chernyshenko, S.I., "Stabilization of trapped vortices by alternating blowing suction," *Physics of Fluids*, Vol. 7, No 4, April 1995, pp. 802-807.
20. Mitchell, A.M. and Delery, J., "Research into Vortex Breakdown Control," *Progress in Aerospace Sciences*, Vol. 37, pp. 385-418, 2001.
21. Gad-el-Hak, M. and Blackwelder, R. F. "Control of the discrete vortices from a delta wing", *AIAA Journal* 25 (8), 1042-1049, 1987.

22. Margalit, S., Greenblatt, D., Seifert, A. and Wygnanski, I., "Delta wing stall and roll control using segmented piezoelectric fluidic actuators," *AIAA Journal of Aircraft*, Vol. 42, No. 3, 2005, pp. 698-709.
23. Guy, Y., Morrow, J. A. and McLaughlin, T.E "Control of vortex breakdown on a delta wing by periodic blowing and suction", AIAA paper 99-0132.
24. Guy, Y., Morrow, J. A. and McLaughlin, T.E "Parametric investigation of the effects of active flow control on the normal force of a delta wing", AIAA paper 2000-0549.
25. Guy Y., Morrow J. A. and McLaughlin T.E "Velocity measurements on a delta wing with periodic blowing and suction", AIAA paper 2000-0550.
26. Siegel S. G., Mclaughlin T. E. and Morrow J. A. "PIV Measurements on a Delta Wing with Periodic Blowing and Suction", AIAA paper 2001-2436.
27. Siegel S. G., Mclaughlin T. E. and Albertson J. A. "Partial Leading Edge Forcing of a Delta Wing At High Angles of Attack", AIAA paper 2002-3268.
28. Gursul, I., Vardaki, E., Margaris, P., and Wang, Z., "Control of Wing Vortices", Notes on Numerical Fluid Mechanics and Multidisciplinary Design, Volume 95, Springer Verlag, New York, 2007, pp. 137-151.
29. Christopher L. Rumsey, C.L., Gatski, T.B, Sellers III, W.L. Vasta, V.N., and Viken, S.A., "Computational fluid dynamics validation workshop on synthetic jets," *AIAA Journal*, Vol. 44, No. 2, 2006, pp. 194-207.
30. Hoffman, J.D and Velkoff, H.R., "Vortex flow over helicopter rotor tips," *AIAA Journal of Aircraft*, Vol. 8, No. 9, 1971, pp. 739-740.
31. Corsiglia, V.R., Schwind, R.G. and Chigier, N. A., "Rapid scanning, three-dimensional hot-wire anemometer surveys of wing-tip vortices," *AIAA Journal of Aircraft*, Vol. 10, No. 12, 1973, pp. 752-757.
32. Greenblatt, D., Nishri, B., Darabi, A. and Wygnanski, I., "Dynamic stall control by periodic excitation. Part 2: Mechanisms," *AIAA Journal of Aircraft*, Vol. 38, No. 3, 2001, pp. 439-447.
33. Seifert, A., Darabi, A. and Wygnanski, I., "Delay of airfoil stall by periodic excitation", *AIAA Journal of Aircraft*, Vol. 33, No. 4, 1996, pp. 691-698.
34. Sullivan, T. M., "The Canadair CL-84 tilt wing design," AIAA Paper 1993-3939, Aircraft Design, Systems and Operations Meeting, Monterey, CA, Aug 11-13, 1993.
35. Manley, D.J., and von Klein, Jr., W., "Design and development of a super-short takeoff and landing transport aircraft," AIAA Paper 2002-6023, 2002 Biennial International Powered Lift Conference and Exhibit, 5-7 November 2002, Williamsburg, VA.
36. Greenblatt, D., "Managing Flap Vortices via Separation Control," *AIAA Journal*, Vol. 44, No. 11, 2006, pp. 2755-2764.
37. Greenblatt, D., Melton, L., Yao, C., Harris, J., "Control of a Wing Tip Vortex" AIAA Paper 2005-4851, 23rd AIAA Applied Aerodynamics Conference, Westin Harbour Castle, Toronto, Ontario, 6-9 June 2005.
38. Greenblatt, D. and Wygnanski, I., "Dynamic stall control by periodic excitation. Part 1: NACA 0015 Parametric Study," *AIAA Journal of Aircraft*, Vol. 38, No. 3, 2001, pp. 430-438.
39. Greenblatt, D., Paschal, K., Yao, C., Harris, J., "A Separation Control CFD Validation Test Case Part 2: Zero Efflux Oscillatory Blowing," *AIAA Journal*, Vol. 44, No. 12, 2006, pp. 2831-2845.

Appendix A: Slot Calibrations

Both leading-edge and flap-shoulder slot calibrations were performed using a hot wire anemometer in the “top-hat” region of the zero mass-flux jets for the frequency range $40 \leq f \leq 400 \text{ Hz}$. Peak slot blowing velocities were averaged for several hundred cycles and these were correlated with unsteady pressure transducer data within the plenums. Both slots were calibrated at 8 spanwise locations, for both standard and swept configurations. Fig. B1 shows averaged peak velocities as a function of rms pressure fluctuations in the plenum for the flap-shoulder slot at mid-semispan ($y/s=0.5$). Due to the geometric similarity of the plenum and slot configurations (see ref. [2]), similar trends were observed for all cases and some representative examples are shown here. Uncertainty intervals are indicated in the figure, namely $\Delta U_j/U_j = \pm 5\%$ corresponding to $\Delta C_\mu/C_\mu = \pm 10\%$, and are based on the hot-wire calibration uncertainty and the uncertainty associated with precise location of the hot-wire within the jet “top-hat” region. It is evident that a linear approximation $U_j \propto p'$, shown on the graph, is adequate to represent the slot perturbations and this was used for all data presented in the body of this paper.

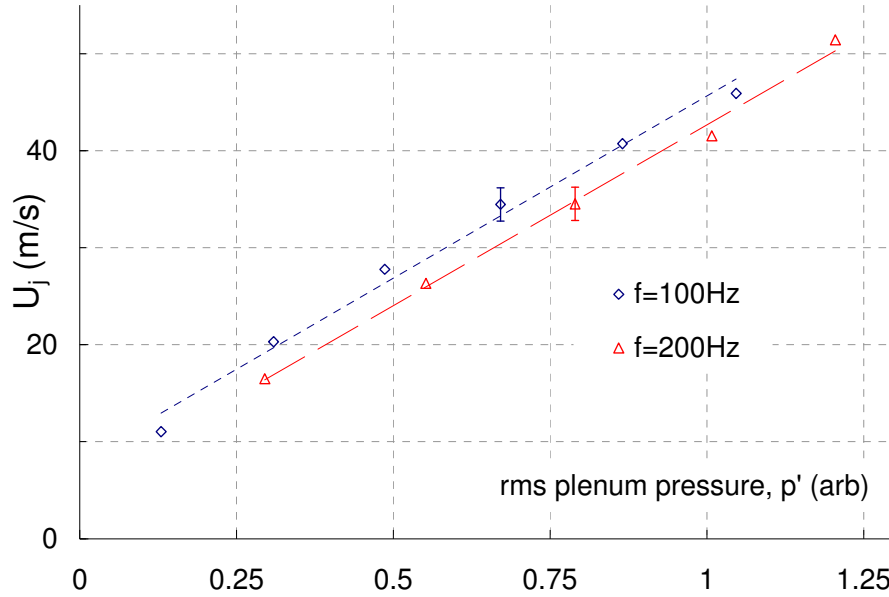


Fig. A1. Average peak blowing velocities as a function of rms pressure fluctuations in the plenum for the flap-shoulder slot at mid-semispan ($y/s=0.5$). Selected uncertainty intervals $\Delta U_j/U_j = \pm 5\%$ are indicated.

Fig. A2 shows the averaged peak slot velocity variation along the span for different frequencies, where the peak jet velocity data is normalized with respect to the maximum value along the span,

which invariably occurs close to the actuator, near the wind tunnel wall. It is seen that the perturbation amplitude decreases with distance from the actuator and the decrease becomes more acute with increasing frequency. Thus increasing frequency clearly has a deleterious effect on the perturbation two-dimensionality. The means by which this problem was minimized is discussed below.

It was ascertained in a previous detailed investigation [16] that the most effective reduced frequencies for NACA 0015 lift enhancement were in the range $0.4 \leq F^+ \leq 0.6$, for both leading-edge and flap-shoulder control. In order to maximize slot flow two-dimensionality and simultaneously attain effective reduced control frequencies, $F^+ = 0.6$ and $F^+ = 0.4$ were predominantly employed at the leading-edge and flap-shoulder, corresponding to approximately $f = 50\text{Hz}$ and $f = 100\text{Hz}$ respectively. Frequencies lower by a factor of $1/\cos A'$ were used for the swept case to account for the lower leading-edge normal velocity (see eqn. 5). The approach outlined above ensured effective active flow control frequencies and adequate perturbation two-dimensionality for both slots, for both standard and swept configurations.

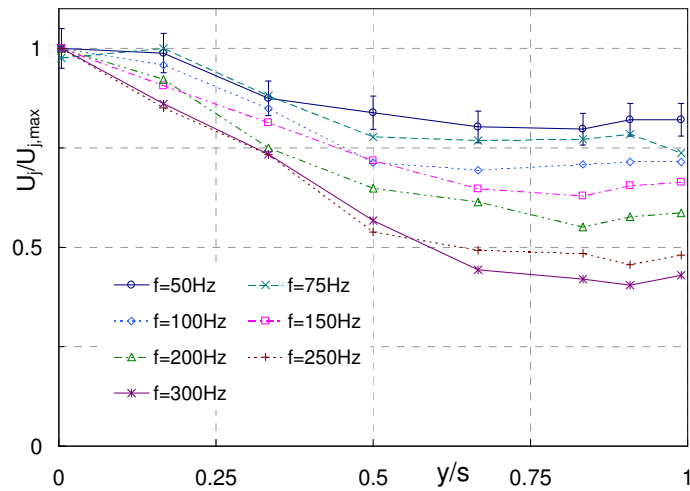


Fig. A2. Average peak blowing velocities from the leading-edge slot, along the span of wing for different frequencies. Selected uncertainty intervals $\Delta U_j/U_j = \pm 5\%$ are indicated.

Appendix B: Pressure Interpolation & Wing Loads

B.1 Pressure Interpolation Method

The model is equipped with 165 static pressure ports arranged in a perpendicular spanwise and chordwise grid. The spanwise ports are located at the chordwise locations $x/c=5/100$, $3/10$, $77/100$, and 1 , and are grouped more closely near the tip. The chordwise ports are located at spanwise locations $y/s=1/6$, $1/2$, $5/6$ and $99/100$, around the perimeter of the wing, and are grouped more closely near the leading-edge.

In order to estimate the wing span-loading more accurately, a three-dimensional interpolation method was employed to determine the chordwise pressures at each of the spanwise locations. Fig. A1 shows locations of pressure ports where the filled symbols represent measured pressures and the open symbols represent interpolated pressures. The interpolation at point (2,2) is performed using the equation of a plane through measured pressures at (1,1), (1,2), and (2,1), namely:

$$C_{P_{2,2}} = \frac{C_{P_{2,1}} - C_{P_{1,1}}}{x_{2,1} - x_{1,1}}(x_{2,2} - x_{1,1}) + \frac{C_{P_{1,2}} - C_{P_{1,1}}}{y_{1,2}^* - y_{1,1}^*}(y_{2,2}^* - y_{1,1}^*) + C_{P_{1,1}} \quad (\text{B1})$$

When the interpolated points are arranged in rectangular grid as shown, equation (B1) reduces to:

$$C_{P_{2,2}} = C_{P_{2,1}} - C_{P_{1,1}} + C_{P_{1,2}} \quad (\text{B2})$$

Similarly, planes are fitted to pressures at points (4,1), (5,1), and (5,2) to obtain those at (4,2), and (3,2) is determined by direct interpolation. An identical procedure to that described above is performed using the pressures at (1,5) to (5,5) to obtain those at (1,4) to (5,4). Finally, pressures at (1,3) to (5,3) are obtained by direct interpolation.

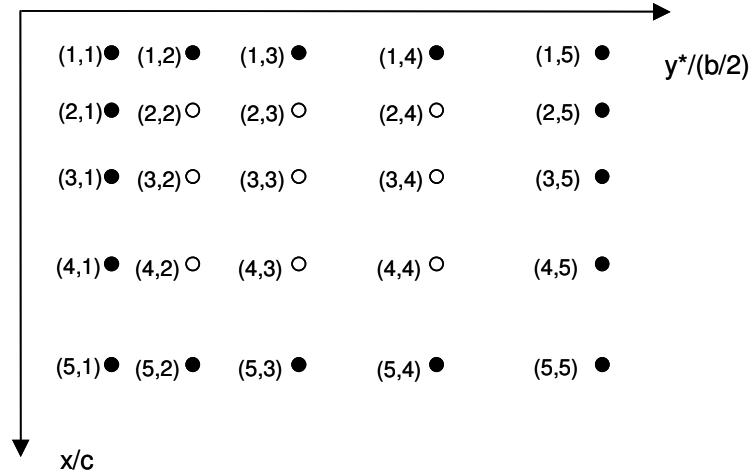


Fig. B1. Schematic illustrating the pressure interpolation method.

B.2 Wing Pressures & Span-Load Variation

Baseline C_L versus α data at two Reynolds numbers, without flap deflections and employing the interpolation method described above, are shown in fig. B2a, and the wing spanwise loading is shown in fig. B2b. Data acquired at even angles are for α increasing and odd angles are for α decreasing. Differences between $Re=500,000$ and $Re=1,000,000$ are minor, for two reasons: firstly the leading-edge slot effectively trips the boundary layer and, secondly, the sharp square wing tip fixes separation on the lower side of the wing independent of Re (see section III.A). Based on the integrated wing loads, stall appears to occur in the vicinity of $\alpha=16^\circ$. However, the spanwise pressures indicate that separation occurs initially inboard at $\alpha=14^\circ$. The distortion of the load distribution near the tip of the wing ($y/s>0.97$) is due to the formation of the tip vortex (see section III.A) and these data are consistent with those of other investigations [9,10] at higher Reynolds numbers and aspect ratios (figs. B3a- B3d). Note that the majority of the pressure data points shown in figs. B3b and B3d were obtained using the interpolation scheme described above in section B1. It is thus evident that the flap slots do not have a noticeable effect on the details of the tip vortex rollup or span loading.

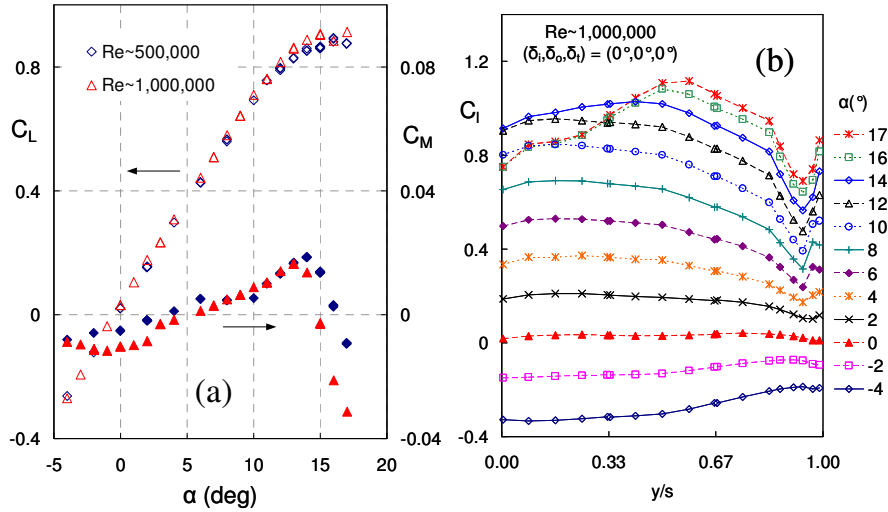


Fig. B2 (a) Unflapped wing lift and moment coefficients for the two Reynolds numbers considered; (b) wing span-loading illustrating formation of the tip vortex on the wing and inboard stall.

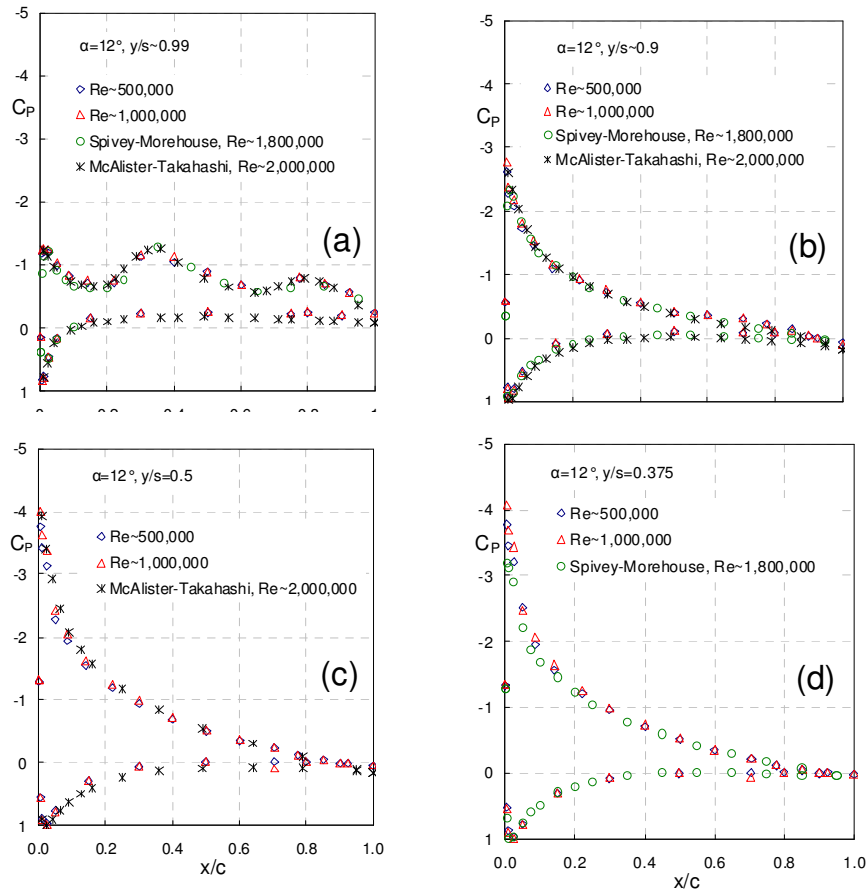


Fig. B3. Sectional pressure distributions compared with previous investigations at higher Reynolds numbers. (Data courtesy of K. W. McAlister [9,10], NASA Ames Research Center).